

Doctor of Philosophy Thesis

**First-principles study of electric field
effects on graphene-based structures for
battery and spintronic materials
application**

Dian Putri Hastuti

MIE UNIVERSITY

Graduate School of Engineering

Division of Materials Science

September 2023

Doctor of Philosophy Thesis

**First-principles study of electric field effects on
graphene-based structures for battery and
spintronics materials application**

グラフェン系物質における電界効果の第一原理計算：
バッテリー材料およびスピントロニクス材料への応用

Dian Putri Hastuti

MIE UNIVERSITY

Graduate School of Engineering

Division of Materials Science

September 2023

Abstract

Two-dimensional (2D) materials have garnered significant attention due to their exceptional properties and potential applications in future electronic devices. However, the extraction of graphene can result in imperfect graphene with defects and impurities that limit its performance, while its lack of a bandgap restricts its application in electronic devices. To overcome the issues, alternately, recent efforts have been carried out to explore ways to use the imperfect graphene in application. One approach involves deliberately introducing defects, such as vacancy defects and interlayer defects, forming heterostructures. Defected graphene has shown promise in increasing the capacity of lithium batteries, while for spintronics applications, combining graphene with materials possessing a larger spin-orbit coupling (SOC), i.e., transition metal dichalcogenides (TMD), is necessary. The purpose of this study is to investigate theoretically defected graphene-based structures and their application in battery and spintronics technologies, where an external electric field, commonly used in semiconductors, is utilized to maximize the capacity of lithium battery and spin generation manipulation for spintronics devices.

The dissertation consists of seven chapters. Chapter one explains the background and purpose of the study. Chapter two describes the methodologies of calculations. We present the method of density functional theory (DFT), which is performed by utilizing full-potential linearized augmented plane wave method within generalize gradient approximation including dispersion correction of van der Waals interaction.

Chapter three focuses on the construction of defected-graphene and germanene to gain understandings of their electronic and structural properties. Investigation included calculating the formation energy of monovacancies in monolayer graphene and monolayer germanene and found that monovacancies in graphene exhibit highly stable with the formation energy of 7.5 eV, while those in germanene are less stable with 2.03 eV. The latter can be attributed to the unique low buckling characteristic of germanene. It

was further conducted on multivacancy in germanene where the most stable multivacancy structures is consisted of even-numbered vacancies. The appropriate structures identified through this study will be used for further calculations.

Chapter four provides an extended study of defected-bilayer graphene evaluating the intercalation of lithium in bilayer graphene, motivated by the need to develop more efficient energy storage systems. In contrast to graphite, which has a lower capacity for lithium storage, bilayer graphene has a higher theoretical capacity due to its larger surface area. The present analysis showed that an external electric field could significantly increase lithium stability in defected-bilayer graphene which led to increase of lithium intercalation to up to 12 atoms. This result shows a 140% increase of capacity of lithium compared to pristine bilayer graphene.

In chapter five, calculations were performed to examine how the electronic structure of graphene-MoS₂ is affected by stacking orientation, element substitution, and interlayer distance. The results indicate that the electronic structures are not significantly influenced by the stacking orientation, in contrast to how element substitution and interlayer distance successfully modify them. Bandgap opening is importantly emerged by forming the heterostructure via a symmetry breaking of carbon staking-sites on MoS₂. The findings are crucial for further research aimed at manipulating the electronic properties of graphene-MoS₂ heterostructure.

In Chapter six, the influence of an external electric field on bandgap opening and spin Hall conductivity in graphene-MoS₂ heterostructure was investigated. As a result, an increase in the electric field induced an out-of-plane polarization, primarily driven by the presence of MoS₂, resulting in insulator to metallic transformation of the heterostructure which led to increase in spin Hall conductivity up to $170 \Omega^{-1} \text{ cm}^{-1}$. These findings demonstrate the potential of spin generation in graphene-MoS₂ heterostructure through spin Hall conductivity, which can be tuned by an electric field. These results open up possibilities for the application of graphene-MoS₂ heterostructure in spintronics applications.

Chapter seven remarks conclusions and prospects of the study.

Acknowledgements

الحمد لله رب العالمين, *All praise be to God, the Lord of the universe.*

I owe a greatest gratitude to Professor Kohji Nakamura, my supervisor at the Graduate School of Engineering, Mie University, for giving me the amazing opportunity to pursue my PhD under his guidance. I am truly thankful for his patience, knowledge, guidance, understanding, and tremendous support, which have been instrumental in helping me complete my studies and write my thesis. I also want to extend my heartfelt thanks for the incredible chances he has given me, such as being a specially appointed assistant professor, an English lecturer at the graduate school of engineering, and a research assistant at the laboratory. These opportunities have allowed me to grow and improve as a researcher. Professor Nakamura, your mentorship has made a profound impact on my academic journey, and I am sincerely grateful for your support.

I am grateful to my committee members for their patience and comments during my preliminary defense, Professor Kohji Nakamura, Professor Hiroshi Murata, Professor Shigeo Kotake, and Professor Hiroshi Yao at the Graduate School of Engineering, Mie University.

I am thankful to the Japanese Government for their generous financial support through Monbukagakusho: MEXT scholarship.

My sincere thanks to Dr. Kenji Nawa, the assistant professor at the MAGN laboratory, for his guidance and advice throughout my research journey. I am truly thankful for the time he dedicated to engaging in meaningful discussions regarding my research progress and providing insights into the life of a PhD student. His support has been in-

credibly meaningful to me. I would also like to express my appreciation to Ms. Harumi Iwano, an administrative staff in the Department of Physics Engineering at Mie University, for her invaluable assistance with the excessive paperwork. Our shared lunches and your kind compliments have always warmed my heart.

I want to convey my deepest appreciation to the entire MAGN group for the incredible memories we have shared both inside and outside the laboratory. From the moment I first arrived in Japan, the MAGN members were the first ones to welcome me, helping me navigate through the adjustment of living in a new country, assisting me with paperwork and making important phone calls. I am immensely grateful for the countless hangouts, home parties, cooking sessions, board game nights, movie marathons, and the unforgettable trips to USJ, Sendai, Aichi for BBQ, and Tokyo with Mana Fukutani, Mayumi Ushida, Yousuke Ozaki, Kazuhiro Matsushita, and Andi Gumarilang. These moments will forever be engraved in my memory.

My heartfelt gratitude to my amazing international student friends at Mie University, especially Yosephine Novita Apriati, Azreen Syazana Nazaruddin, and Anysia Hedy Ujat. You guys kept me sane throughout my doctoral study and our memories together are etched not only in my heart but also in my Agoda booking history. A special shoutout goes to Farah Zayanah and her family, as well as the awesome 'Takoyaki Group,' for their constant help, inviting me to home parties, Raya celebration, and including me in last-minute plans. Thanks to all of you, Japan truly feels like a safe and cozy home for me. I am immensely grateful for the unforgettable moments we have shared during my time at Mie University.

I would like to extend my heartfelt gratitude to my family for their unwavering support, both mentally and financially, throughout my journey. Your belief in me and my choices, and granting me the freedom to live the life I desire, mean the world to me. I also want to express my deepest appreciation to my (late) grandparents from my mother's side, whose constant motivation and contributions have shaped the path I have chosen. I am forever indebted to my grandfather and grandmother in Yogyakarta, who unfortunately passed away while I was studying in Japan, and I deeply regret not being able to be with them in their final moments. I dedicate this dissertation to all of them as a token of my love and remembrance.

Contents

Abstract	i
Acknowledgements	iii
Contents	vii
List of Figures	x
List of Tables	xi
1 Introduction	1
1.1 Background	1
1.1.1 Graphene and other two dimensional materials	1
1.1.2 Demand for application of graphene-based structures	2
1.1.2.1 Battery	2
1.1.2.2 Spintronics	3
1.1.3 Problems and challenges	4
1.2 Purpose of study	6
1.3 Outline of the doctoral thesis	7
2 Theory and Methods	8
2.1 Density functional theory	8
2.1.1 Basis of Density Functional Theory	8
2.1.2 The Hohenberg-Kohn theorem	9
2.1.3 Kohn-Sham theorem	10
2.2 Exchange and correlation functional	11
2.2.1 Local density approximation (LDA)	11
2.2.2 Generalized gradient approximation (GGA)	12
2.3 Full linearized augmented plane wave	12

2.4	Grimme's van der Waals corrections	13
3	Graphene and other two-dimensional materials	16
3.1	Introduction	16
3.1.1	Graphene	16
3.1.2	Germanene	16
3.1.3	TMD materials	17
3.2	Calculation Model	17
3.3	Structure of 2D materials	17
3.4	Electronic structure	21
3.5	Vacancy	21
3.6	Concluding Remarks	25
4	Lithium intercalation in bilayer graphene	27
4.1	Introduction	27
4.2	Calculation Model	28
4.3	Bilayer graphene structure stability	29
4.4	Intercalation and capacity	35
4.5	Concluding Remarks	37
5	Graphene-MoS₂heterostructure	38
5.1	Introduction	38
5.2	Calculation Model	39
5.3	Stacking orientation, element substitution, and interlayer distance effect on the electronic structures	40
5.3.1	Stacking orientation	40
5.3.2	Dependence of element substitution	42
5.3.3	Dependence of interlayer distance	44
5.4	Concluding Remarks	46
6	Graphene-MoS₂heterostructure with external electric field	47
6.1	Introduction	47
6.2	Calculation Model	48
6.3	Electric polarization and electron density	50
6.4	Electronic structure	52

6.5 Spin Hall Conductivity	54
6.6 Concluding Remarks	57
7 Conclusions and prospects	59
Bibliography	61
List of Publications	78
List of Presentations	79

List of Figures

2.1	DFT-based calculation flowchart for the self-consistent field, beginning from setting initial charge density, $n(r)$ and the convergency will be acquired when $n(r)$ equals $n(r)^{new}$	15
3.1	The structure of monolayer graphene	18
3.2	Supercell of germanene	18
3.3	Low-buckled system of germanene	19
3.4	Top view of monolayer MoS ₂ where blue and silver colored atoms represent Mo and S atom respectively.	19
3.5	Top view of monolayer MoSe ₂ where blue and green colored atoms represent Mo and Se atom respectively.	20
3.6	Top view of monolayer MoTe ₂ where blue and gold colored atoms represent Mo and Te atom respectively.	20
3.7	Band structure of (a) graphene, (b) MoS ₂ , (c) MoSe ₂ , and (d) MoTe ₂	21
3.8	Monovacancy in monolayer (a) graphene and (b) germanene	22
3.9	Relaxed structure of germanene (a) monovacancy and (b) divacancy	24
3.10	Relaxed structure of germanene (a) tri-, (b) tetra-, (c) penta-, (d) hexa-, (e) hepta-, and (f) octavacancy.	25
4.1	Graphene bilayer structure of (a) top and side view of AB stacking, (b) top and side view AA stacking, (c) top and side view of lithium inserted into defected bilayer graphene, and (d) the arrangement of external electric field applied perpendicularly to the system. Red and Pink-colored atoms represent the top and bottom layer of the bilayer configuration, respectively. In AB stacking half of carbon atoms in the bottom layer are located at the hollow site of top layer while in AA configuration, top and bottom layers are perfectly aligned.	30

4.2	Band structure and DOS of (a) pristine AA stacking, (b) pristine AB stacking, (c) defected AA stacking, and (d) defected AB stacking. Additional bands emerged at fermi level in vacancy structures are represented by pink colored bands.	32
4.3	Adsorption energy in fuction of (a) position of lithium and (b) external electric field. The insets in (a) illustrate the position of lithium inserted into the bilayer graphene correspond to P1 to P6, where P4 refers to the position of lithium exactly under the defect site and P6 represents the furthest position from the defect site.	34
4.4	Charge density with lithium inserted into defected bilayer graphene. . .	35
4.5	Intercalation energy in function of number of lithium atom inserted into the system. Zero is the threshold for the maximum amount of lithium atom can be accomodated into the system.	36
5.1	Calculated band structures of graphene-MoS ₂ , graphene-MoSe ₂ , and graphene-MoTe ₂	40
5.2	Band structures and DOSs of graphene-MoS ₂ heterostructures under different structure arrangements: (a) 1:1 structure with C _S stacking orientation, (b) 1:1 heterostructure with C _{Mo} stacking orientation, (c) 4:3 structure with C _S stacking orientation, and (d) 4:3 structure with C _{Mo} stacking orientation. The insets show a bandgap at K in each structure	42
5.3	Charge density of 1:1 structure (a) C _{Mo} stacking orientation and (b) C _S stacking orientation. The yellow color shows positive charges	42
5.4	Calculated band structures of graphene-MoS ₂ , graphene-MoSe ₂ , and graphene-MoTe ₂	44
5.5	Calculated DOSs of graphene-MoS ₂ , graphene-MoSe ₂ , and graphene-MoTe ₂	44
5.6	Binding energy as a function of interlayer distance	45
5.7	Bandgap in function of interlayer distance	46

6.1	(a) and (b) Side and bottom views of graphene-MoS ₂ heterostructure where blue, silver, and red colors represent Mo, S, and C atoms, respectively. An external electric field is applied along the surface normal where a positive electric field is defined by a grey arrow in (a). (c) A 2D Brillouin zone of graphene-MoS ₂ heterostructure and symbols represent high symmetry \mathbf{k} -points used in the present work.	49
6.2	(a)-(d) Bandgap, electric polarization, spin Hall conductivity, and energy of eigen states as a function of electric field from -0.26 to 0.51 V/Å. In (d), red open circles and blue closed circles represent the spin-down and spin-up states around Fermi level at K, and white, blue, and orange vertical shades indicate electronic states of insulator, n -type metal, and p -type metal states, respectively.	50
6.3	Electron density distribution of heterostructure for external electric fields of (a) -0.26 V/Å, (b) 0.00 V/Å, and (c) 0.26 V/Å, which show contrast reaction for negative and positive electric fields. Yellow color represents an accumulation of electrons while the blue color shows an electron depletion with an absolute value of 10^{-5} electrons/Bohr ³	52
6.4	The left and right figures represent calculated band structure and Dirac points at K and K', respectively, for electric fields of (a) -0.26 V/Å, (b) 0.00 V/Å, and (c) 0.26 V/Å. Green shades on the left figures show the weight of wavefunction of MoS ₂ . Red and blue circles in the right figures represent the spin-down and spin-up states projected along to the surface normal.	54
6.5	\mathbf{k} -dependence of spin Hall conductivity for external electric fields of (a) -0.26 V/Å, (b) 0.00 V/Å, and (c) 0.26 V/Å. The positive and negative peaks are found at K and K', associated with the location of Dirac points.	56
6.6	Band structure around K (top) and corresponding spin Berry curvature $\Omega_{yx,m}^s$ (bottom) under electric fields of (a) 0.13, (b) 0.26, (c) 0.36, (d) 0.51 V/Å, where numbers (25 and 26) indicate band indexes (m). In top panels, blue and red circles represent the spin-up and -down states, and in bottom panels, blue and red lines represent spin Berry curvature in Eq. (2) of concerned bands. Zero energy sets to an energy of the valence edge.	57

List of Tables

1.1	Potential applications of graphene, germanene, and TMDs	2
1.2	Potential applications of Heterostructure	6
3.1	Formation energies E_f and the dissociation energies E_d (in eV) of the V1 to V8.	24
4.1	Number of lithium atom that can be accommodated in the system (N_{Li} , composition of lithium atom per number of carbon atom (C_{Li}), and capacity of each structure.	37
5.1	Calculated interlayer distance (d) and bandgap ΔE of graphene-MoS ₂ and graphene-MoSe ₂	44

Chapter 1

Introduction

1.1 Background

1.1.1 Graphene and other two dimensional materials

Graphene is a two-dimensional (2D) material consisting of a single layer of carbon atoms arranged in a planar honeycomb lattice structure[1, 2, 3]. Graphene is a thinnest material, with a thickness of 0.334 nm. Since its discovery in 2004 [1], it has received significant attention in the scientific community due to its remarkable properties such as high mobility charge transport of $1 \times 10^4 \text{ cm}^2\text{V}^{-1}\text{s}^{-1}$ at room temperature [4]. Each layer of graphene has been found to absorb up to 2.3% of white light with a reflectance of less than 0.1%, and as a result, the pure single graphene layer exhibits high transparency and flexibility [5]. By using nanoindentation in an AFM to measure the mechanical characteristics of free-standing monolayer graphene, Hone et al. [6] reported the intrinsic strength of the monolayer membrane to be 42 N m^{-1} and determined that graphene was "the strongest material ever measured". Graphene has potential applications in biomedical field such as drug delivery and diagnostic technology [7, 8]. A polymer composite with a vertically stacked graphene design was also reported by Han et al. in 2020. Due to its high thermal conductivity of $2.18 \text{ W m}^{-1}\text{K}^{-1}$, this substance is a promising candidate for thermal interface materials[9].

Many scientists are now searching for other 2D materials as a result of graphene's impressive rise to fame. This new area of 2D materials is still being explored, its potential for new physics and devices is still largely unrealized, and its properties have not yet been properly understood. The group IV materials are the most obvious alternatives to graphene. Other member of group IV A which is interesting to explore is

germanene. However, in contrast to graphene, germanene's atoms are connected to one another through sp^3 hybrid orbitals, which are more stable than sp^2 hybrid orbitals. In their bulk phase, they do not exhibit a van der Waals layered structure[10]. Synthesizing of germanene can be done by $CaGe_2$ -based chemical exfoliation and vacuum deposition[11, 12]. Germanene exhibits many unique properties, such as structural stability[13], semi-metallic behavior[14], large carrier mobility[15], spin-polarized electronic transport[16], and controllable magnetic properties[17].

Another interesting group of materials is transition-metal dichalcogenides (TMD). TMD has attracted significant attention in recent years and are being massively researched for use in photoelectronic devices due to a wide range of electronic, optical, mechanical, chemical, and thermal properties[18]. Many 2D TMDs, unlike graphene, are semiconductors in nature and have the potential to be made into ultra-small, low-power transistors that are more effective than current silicon-based transistors struggling to keep up with the demand from ever-smaller devices[19]. TMD is a desired group of materials due to their outstanding properties in potential utilization, such as for electronic devices, optoelectronic devices [20], gas sensing[21] and energy storage [22].

The potential applications of related 2D materials are presented on the table below.

Table 1.1: Potential applications of graphene, germanene, and TMDs

Material	Properties	Potential Applications
Graphene	Efficiency at 12.5 % and 250-W power output	Solar cell [23]
Graphene	mobility 130,000 cm^2	Spintronics transistor[24]
Germanene	Air stability, bandgap of 1.57 eV	lithium batteries[25]
Germanene	High thermal stability	Optoelectronic devices[26]
MoS ₂	Photosensing (photodetector)	Excellent electronic and optical properties[27]
MoSe ₂	High specific capacity	Energy storage[28]
MoTe ₂	High responsivity	Photodetectors[29]

1.1.2 Demand for application of graphene-based structures

1.1.2.1 Battery

The development of high-performance energy storage systems is critical for addressing global energy challenges, and lithium-ion batteries (LIBs) are favorable choice due to their high energy density and long cycle life. However, the limited capacity of

graphite of 372 mAhg^{-1} , the traditional anode material in LIBs, has prompted research into alternative materials. Bilayer graphene is a two-dimensional material with high electronic conductivity and high specific surface area, making it a potential candidate for use as an anode material in LIBs.

Recent studies have shown that bilayer graphene can exhibit high lithium-ion storage capacity, making it an attractive alternative to graphite[30, 31]. According to a study [32], a composite anode composed of graphene and SnO_2 demonstrated an impressive reversible capacity of 800 mAhg^{-1} after undergoing 100 cycles. Additionally, another study [33] found that a composite anode consisting of graphene and SiO exhibited a remarkable reversible capacity of 1000 mAhg^{-1} after the same number of cycles.

1.1.2.2 Spintronics

Spintronics, harnesses the spin property of electrons to create innovative devices for information processing and storage. Graphene, a two-dimensional lattice of carbon atoms, has garnered significant attention in spintronics due to its exceptional electronic and mechanical properties, as well as its unique spin transport characteristics. With its long spin relaxation time, high carrier mobility, and tunable spin properties in heterostructures, graphene offers efficient spin manipulation and transport, enabling the development of high-performance spintronic devices[34]. By exploring graphene-based structures and their spin-dependent phenomena, researchers are paving the way for advancements in spintronics technology, unlocking the potential for next-generation spin-based devices with enhanced functionality and energy efficiency.

Graphene, with its low intrinsic spin-orbit coupling (SOC), stands in contrast to TMDs, which possess larger intrinsic SOC [35]. In recent years, extensive research has been conducted on the proximity-induced SOC in graphene by TMDs, particularly in the context of a graphene- MoS_2 heterostructure, where a reported Rashba SOC strength of 0.9 meV was observed [36]. Dankert and Dash demonstrated the successful manipulation of spin current, spin lifetime, and the Schottky barrier in graphene- MoS_2 through electric gate control [34]. Omar and van Wees achieved spin injection into graphene by utilizing a WS_2 layer and were able to tune the interface resistance and spin injection efficiency through the application of a voltage bias between the layers [37]. Another study reported the observation of a non-zero bandgap of 17 meV in the

graphene-WS₂ system [38]. The Spin Hall effect (SHE), which generates a transverse spin current and facilitates charge-to-spin conversion, has been extensively investigated [39, 40, 41].

1.1.3 Problems and challenges

Despite the excellent properties and wide range of applications of graphene-based structures, it is important to acknowledge that they are not yet perfect. Several problems and challenges still need to be addressed in order to fully exploit their potential. Firstly, imperfections and defects in graphene, which exist in reality, can affect its performance and reliability. These imperfections can arise during the manufacturing process or as a result of environmental factors, leading to decreased efficiency and functionality. Secondly, the lack of a bandgap in graphene poses a significant limitation for certain applications that require control over electrical conductivity. The absence of a bandgap restricts the modulation of current flow, limiting its suitability for electronic devices. Lastly, there are ongoing challenges in tuning graphene-based structures to enhance their quality and overcome their inherent limitations. This involves manipulate the properties of graphene. Addressing these challenges and finding effective solutions will undoubtedly contribute to the further advancement and widespread implementation of graphene-based structures in various industries and technologies.

Defects in 2D materials can be categorized into point defects and interlayer defects. Point defects involve localized deviations in the lattice structure and include vacancies, adatoms, substitutional impurities, and interstitial atoms. Vacancies result from the absence of atoms at specific lattice sites and can affect the material's mechanical, electrical, and optical properties. Adatoms are atoms residing on the surface, altering the electronic structure and reactivity. Substitutional impurities and interstitial atoms occur when foreign atoms occupy lattice sites or fill spaces between them, respectively, leading to changes in the material's behavior.

Interlayer defects, on the other hand, occur between the layers of multi-layered 2D materials. They comprise dislocations, grain boundaries, and stacking faults. Dislocations are line defects arising from atom arrangement mismatches between adjacent layers, influencing mechanical strength and electronic properties. Grain boundaries form at the meeting points of regions with different orientations, affecting transport properties and mobility of charge carriers. Stacking faults occur due to deviations

from the regular stacking sequence of atomic layers, significantly impacting electronic structure and optical properties.

While various types of defects exist, this research paper particularly focuses on two examples: vacancy defects as point defects and van der Waals (vdW) heterostructures as interlayer defects. Understanding and controlling these defects in 2D materials, such as vdW heterostructures, are crucial for harnessing their potential in diverse applications.

Vacancy defect can occur naturally due to imperfect process. Artificial vacancy defect is also common practice way to tune properties of the materials. Previous study reported that by creating vacancy defect, multiple properties are tunable such as vacancy defects can be used to modify the electronic and magnetic properties of armchair graphene nanoribbons [42].

In term of heterostructure, we can isolate 2D monolayer and restack them into any stacking heterostructure thanks to the weak van der Waals (vdW) interlayer force without having to take into account atomic commensurability as in their bulk equivalents. Consequently, heterostructure made of 2D layered materials have become a new area of study[43]. Mechanical stacking can create the vertically stacked 2D layers, which is a quick and practical method to create heterostructures. Additionally, over the past few years, the field of 2D heterojunction fabrication techniques using chemical vapor deposition (CVD) has grown. The CVD method also produces large-area 2D materials for mechanical assembly. Additionally, different stacking structures can grow immediately. The synthetic heterojunction can offer a much cleaner interface for theoretical work, leading to improved device performance[44].

Two-dimensional (2D) heterostructures, composed of atomically thin materials stacked together, have attracted significant research attention due to their unique electronic, optical, and mechanical properties. These properties are distinct from those of their individual constituent materials and can be tailored by selecting appropriate materials and stacking configurations. Therefore, research in 2D heterostructures has the potential to lead to breakthroughs in the fields of electronics, photonics, and many more as presente in the table below.

Addressing the importance of tuning graphene-based structures, it is worth noting that various methods have been explored in the semiconductor field, such as doping and applying electric fields, to modify the properties of materials. However, in this study, the focus will be on tuning graphene by means of electric fields. Electric field

Table 1.2: Potential applications of Heterostructure

Material	Properties	Potential Applications
graphene-MoS ₂	Improvement ON/OFF ratio	Vertical FETs[45]
graphene-MoS ₂	Photogain > 10 ⁸	Photodetector[46]
graphene-MoS ₂ /graphene	External quantum efficiency 55%	Photodetector[47]
Graphene/WS ₂	Improvement on efficiency	Solar cells[48]
WSe ₂ /MoSe ₂	Improvement on efficiency	Solar cells[49]
WS ₂ /MoS ₂	Power conversion efficiency 0.2%	Solar cells[50]
graphene-MoTe ₂ /graphene	High photoresponsivity	Photodetector[51]

tuning offers a promising avenue for controlling and manipulating the properties of graphene. By applying an external electric field, it becomes possible to modulate the band structure, induce a bandgap, and tailor the electrical conductivity of graphene.

The electronic properties of graphene-based structures can be significantly influenced by the application of an external electric field. Research has demonstrated that the interlayer distance and the perpendicular electric field can be controlled to tune the electronic properties of graphene/graphene-like germanium carbide van der Waals heterostructures[52]. Additionally, external electric fields have proven effective in modulating the band gap of graphene/g-C₃N₄ bilayers[53]. Moreover, the application of an external electric field has shown to have a notable impact on the spin lifetime magnitudes and anisotropies in graphene layers, as well as on the carrier density[54]. These findings highlight the ability of electric fields to serve as a powerful tool for precisely adjusting and tailoring the electronic and spin properties of graphene-based structures, offering opportunities for enhancing their performance and enabling novel functionalities in various electronic and spintronic devices.

1.2 Purpose of study

This thesis has three main objectives, firstly understanding electronic structure affected by electric field in graphene-based structures. Second, investigating electric field effect in defected-graphene structures and application to lithium-battery anode and third, electric field effect in graphene-MoS₂ heterostructure and application to spin generation via spin Hall conductivity.

1.3 Outline of the doctoral thesis

This doctoral thesis consists of seven chapters. In Chapter 1, the background of this research is introduced. The explanation of the theory and application of density functional theory in Chapter 2. In Chapter 3, vacancy structures of graphene and germanene are presented. Chapter 4 covers the discussion lithium intercalation in defected-bilayer graphene in electric field. In Chapter 5, the investigation of the graphene-MoS₂ heterostructure and the effect of stacking orientation, element substitution, and interlayer distance were presented. Chapter 6 covers discuss the external electric effect on bandgap and spin Hall conductivity in the graphene-MoS₂ heterostructure. Finally, the summary is provided in Chapter 7.

Chapter 2

Theory and Methods

2.1 Density functional theory

2.1.1 Basis of Density Functional Theory

A fully interacting Schrödinger equation of a complex system consisting of many electrons and nuclei is given by[55]:

$$\hat{H}\Psi(\mathbf{r}_1, \mathbf{R}_1, \mathbf{r}_2, \mathbf{R}_2, \dots, \mathbf{r}_N, \mathbf{R}_N) = E\Psi(\mathbf{r}_1, \mathbf{R}_1, \mathbf{r}_2, \mathbf{R}_2, \dots, \mathbf{r}_N, \mathbf{R}_N) \quad (2.1)$$

where \hat{H} is Hamiltonian operator and E is eigen value representing a total energy of the system. $\mathbf{R}_1, \mathbf{R}_2, \dots, \mathbf{R}_N$ and $\mathbf{r}_1, \mathbf{r}_2, \dots, \mathbf{r}_N$ are cartesian positions of nuclei and electrons, respectively. The Hamiltonian operator \hat{H} is expressed as:

$$\hat{H} = \hat{T}_e + \hat{T}_n + \hat{V}_{ee} + \hat{V}_{nn} + \hat{V}_{en} \quad (2.2)$$

where \hat{T}_e is many-electrons kinetic energy operator, \hat{T}_n is many-nuclei and kinetic energy operator, \hat{V}_{ee} is electron-electron interaction energy operator, \hat{V}_{nn} is nucleus-nucleus interaction energy operator, and \hat{V}_{en} is electron-nucleus interaction energy operator.

The kinetic energy operators are expressed as follows:

$$\hat{T}_e = -\frac{\hbar^2}{2} \sum_i^N \frac{1}{m} \nabla_i^2(\mathbf{r}_i), \quad (2.3)$$

$$\hat{T}_n = -\frac{\hbar^2}{2} \sum_i^N \frac{1}{M} \nabla_i^2(\mathbf{R}_i), \quad (2.4)$$

and the interaction energy operators are expressed as:

$$\hat{V}_{ee} = \frac{e^2}{2} \sum_{i \neq j} \frac{1}{|\mathbf{r}_i - \mathbf{r}_j|}, \quad (2.5)$$

$$\widehat{V}_{nn} = \frac{e^2}{2} \sum_{i \neq j} \frac{Z_i Z_j}{|\mathbf{R}_i - \mathbf{R}_j|}, \quad (2.6)$$

$$\widehat{V}_{en} = -e^2 \sum_{i,j} \frac{Z_j}{|\mathbf{r}_i - \mathbf{R}_j|}, \quad (2.7)$$

where M_i and Z_i are mass of the i -th nucleus and atomic number, respectively. Except for the hydrogen atom, where only one electron and one proton interact, it is extremely difficult to solve the Schrödinger equation (Eq. 2.1) that describes the behavior of electrons and nuclei interacting through their electrostatic Coulomb interaction. To address this challenge for many-body systems, various methods have been developed. One widely recognized approach is the Born-Oppenheimer approximation[56]. The ground state characteristics can be deduced from the ground state electron charge densities according to the density functional theory (DFT), which was created by Hohenberg and Kohn in 1964 [57]. The degree of freedom is significantly decreased from $3N$ dimensions to only 3, which is an essential advantage.

2.1.2 The Hohenberg-Kohn theorem

The work of Hohenberg and Kohn can be resumed as two important theorems. These theorems provide technics to determine the Hamiltonian operator and the properties of the system based on electron density. The electronic density $n(\mathbf{r})$ is given by

$$n(\mathbf{r}) = N \sum_{s_1} \sum_{s_2} \dots \sum_{s_N} \int \dots \int |\Psi(r_1, s_1, r_2, s_2, \dots, r_N, s_N)|^2 dr_1 dr_2 \dots dr_N, \quad (2.8)$$

and

$$\int n(\mathbf{r}) d\mathbf{r} = N. \quad (2.9)$$

Theorem I. (Hohenberg-Kohn 1) In external potential of interacting particles for any system $v_{ext}(\mathbf{r})$, the potential $v_{ext}(\mathbf{r})$ is determined uniquely by the ground state particle density $n_0(\mathbf{r})$.

Theorem II. (Hohenberg-Kohn 2) For any particular $v_{ext}(\mathbf{r})$, the exact ground state energy of system is a global minimum value of this functional, and the density $n(\mathbf{r})$ that minimizes the functional is the exact ground state density $n_0(\mathbf{r})$.

In a spin-polarized system, the ground state's total energy and other properties can be determined using a functional that depends on the spin densities. Typically, the spin densities are represented as four-component spinors. However, in simpler cases like

collinear magnetic systems, the total energy of the spin-up and spin-down densities, n^\uparrow and n^\downarrow can be described as

$$E = E[n^\uparrow, n^\downarrow]. \quad (2.10)$$

According to this theorem, the total energy of considered system is

$$E[n] = T[n] + E_H[n] + V_{ext}[n] + (\text{non-classical term}), \quad (2.11)$$

where the first term, $T[n]$, is a kinetic energy of interacting electrons, the second one, $E_H[n]$, is Hartree energy which counts the Coulomb interaction of electron charge density including the contribution from itself, and the third one, $V_{ext}[n]$, is an external potential given by

$$V_{ext}[n] = \int n(\mathbf{r})v_{ext}(\mathbf{r})d\mathbf{r}. \quad (2.12)$$

The Hohenberg-Kohn theorem, however, was unable to give a precise representation of the total energy functional, particularly the kinetic term of interacting electrons. A sufficient number of precise approximations must be found in order for DFT to be useful. One year after Hohenberg and Kohn's theorem was first proposed, this problem was resolved by Kohn and Sham.

2.1.3 Kohn-Sham theorem

By assuming a system in which electrons move freely but experience an effective potential, they replaced the kinetic contributions of interacting electrons with those of non-interacting ones. Even under this bold assumption, the non-interacting kinetic term can be accurately calculated and comprises the majority of the exact $T[n]$ in Eq. (2.11).

To strictly formulated total energy, which has unknown part, $E_{xc}[n]$, is expressed by

$$E[n] = T_s[n] + E_H[n] + V_{ext}[n] + E_{xc}[n]. \quad (2.13)$$

T_s denotes the kinetic energy under the non-interacting assumption,

$$T_s[n(r)] = \sum_{i=1}^N \left\langle \psi_i(\mathbf{r}) \left| -\frac{1}{2}\delta_i^2 \right| \psi_i(\mathbf{r}) \right\rangle \quad (2.14)$$

This method employed variational principle implied by a minimum property of energy functional to derive a single-particle Schrödinger equation. In this method, the ground state density is assumed in a non-interacting system, which is given by:

$$n(\mathbf{r}) = \sum_i^N |\psi_i(\mathbf{r})|^2 \quad (2.15)$$

Kohn-Sham equation is derived as:

$$\left(-\frac{\nabla^2}{2} + V_{KS}(\mathbf{r}) \right) \psi_i(\mathbf{r}) = \epsilon_i \psi_i(\mathbf{r}), \quad (2.16)$$

where V_{KS} is Kohn-Sham potential, which is given as:

$$V_{KS}(\mathbf{r}) = V_{ext}(\mathbf{r}) + V_H(\mathbf{r}) + V_{xc}(\mathbf{r}) \quad (2.17)$$

External, Hartree, and exchange-correlation potentials are represented, respectively, by V_{ext} , V_H , and V_{xc} . Kohn-Sham potential V_{KS} is first calculated using an initial electron density, which is determined by superimposing atomic electron density distributions. The Kohn-Sham equation is then resolved. The sum of energies and a new charge density are deduced from the eigenvalues and eigenfunctions. The new guest of electron density is used to compute the new V_{KS} if they have not yet converged. After that, this process is repeated until convergence is achieved.

2.2 Exchange and correlation functional

The many-body problems are re-written as an effective one- electron problem by using Kohn-Sham equation. However, Kohn-Sham equation is unable to be solved since the derivative of $E_{xc}[n(\mathbf{r})]$ is unknown. Therefore, it is a need to have an accurate exchange-correlation energy $E_{ex}[n(\mathbf{r})]$ or potential $V_{xc}(\mathbf{r})$ functional in order to give a satisfactory description of realistic condensed-matter systems. The familiar exchange-correlation functionals widely used are local density approximation (LDA) and generalized gradient approximation (GGA) functionals that we are going to discuss in the next section.

2.2.1 Local density approximation (LDA)

Since the functional $E_{xc}[n(\mathbf{r})]$ is unknown, one has to find a good approximation for it. A simple approximation based on homogeneous electron gas (HEG), which was

suggested by Hohenberg and Kohn, is LDA. The exchange-correlation potential $V_{xc}(\mathbf{r})$ in LDA is given by

$$\frac{\delta E_{xc}[n]}{\delta n(\mathbf{r})} = \int d\mathbf{r} \left[\epsilon_{xc} + n \frac{\partial \epsilon_{xc}}{\partial n} \right] \quad (2.18)$$

$$V_{xc}(\mathbf{r}) = \epsilon_{xc}([n], \mathbf{r}) \quad (2.19)$$

where $\epsilon_{xc}([n], \mathbf{r})$ is an energy function per electron that depends on the density $n(r)$ only.

2.2.2 Generalized gradient approximation (GGA)

As previously mentioned, LDA is employed as a strategy for approaching a homogeneous electron gas. Assuming an inhomogeneous density, we must introduce generalized gradient approximation (GGA), which expands electronic density in terms of gradient and higher order derivatives. While GGA remains local, it also takes into account the gradient of electron density at the same coordinate.

2.3 Full linearized augmented plane wave

Kohn-Sham equations can be solved in a variety of ways. The basis function for wavefunction satisfying the Bloch boundary condition is chosen as a set of plane waves in order to solve Kohn-Sham equations for periodic crystal systems. An unit cell is divided into two distinct regions in Slater's augmented plane-wave (APW) methods [58]: one region is a sphere known as the muffin tin (MT) region, and the other is known as the interstitial region. The energy dependence of wavefunction, which results in a nonlinear eigenvalue problem, is a drawback of the APW method.

The linear APW (LAPW) approach was suggested by Andersen[59], Koelling, and Arberman [60] to address this issue. The LAPW approaches work by leveraging the Taylor expansion of a radial function to give the basis inside the MT more variational freedom. Applying the LAPW methods to surfaces, which have open structures, is challenging. The potential used in a Hamiltonian was approximated using shape in both the APW and LAPW approaches.

By combining the selection of the LAPW basis set with the treatment of charge density and full potential without any form approximations inside the muffin-tin spheres and interstitial region, Hamman and Wimmer [61, 62] formulated full-potential LAPW

method (FLAPW). Because of an inclusion of the warped interstitial $\sum V_I^G e^{iGr}$ and the non-spherical term inside the MT spheres, the interstitial potential V_I^0 and the spherical MT approximation $V_{MT}^0(r)$ are relaxed to reach this generalization:

$$V(\mathbf{r}) = \left\{ \begin{array}{ll} \sum_G \sum_G V_I^G e^{iGr} & \text{interstitial region} \\ \sum_L V_{MT}^L(r) Y_L(\mathbf{r}) & \text{muffin-tin} \end{array} \right\} \quad (2.20)$$

In this context, L represents the quantum numbers l and m , while G represents all reciprocal lattice vectors up to the maximum value of K_{\max} . The term Y_L denotes the spherical harmonics. For accurate electronic structure calculations, the FLAPW (Full-Potential Linearized Augmented Plane Wave) method is the preferred approach. In this study, a FLAPW code developed by Nakamura et al. [63] has been utilized.

2.4 Grimme's van der Waals corrections

In small molecular systems, chemical bondings are the key factor, but as the size of the system increases, its significance diminishes. They are held together by electrostatic and polarization interactions. It would be beneficial to develop a mechanism for their description because crystalline materials with strong van der Waals interactions make up a significant portion of systems examined with DFT. As previously indicated, effects from dynamical correlations between changing charge distributions could not be accurately simulated by standard density functionals.

Although there has been significant progress in developing a totally ab-initio treatment of dispersion forces, it is currently still too computationally expensive to be employed frequently on larger systems. So, in DFT, attempts were made to alter current density functionals, with GGA leading the way, the so-called DFT+D-approach (plus dispersion), which combines traditional DFT-functionals with an additional energy term, is perhaps the most promising contender to come out of this regime. In essence it simply adds a semiempirical dispersion potential to the conventional Kohn-Sham total energy as:

$$E_{DFT+D} = E_{KS} + E_{disp} \quad (2.21)$$

where E_{disp} is dispersion Energy.

For a periodic (crystalline) N -atom system, is defined by:

$$E_{disp} = -s_6 \sum_{ij}^N \sum_L \frac{C_6^{ij}}{(|\mathbf{r}_{i,0} - \mathbf{r}_{j,L}|)} \quad (2.22)$$

where $\mathbf{L} = (l_1, l_2, l_3)$ sums all translations of the unit cell, s_6 is a global scaling-factor, $C_6^{i,j}$ represents the dispersion coefficient for atom pair ij , $\mathbf{r}_{i,0}$ is the position vector of atom i in the unit cell at $\mathbf{0}$ and $\mathbf{r}_{j,L}$ while $f(|\mathbf{r}_{i,0} - \mathbf{r}_{j,L}|)$ is a damping function as defined as:

$$f(|\mathbf{r}_{i,0} - \mathbf{r}_{j,L}|) = \frac{1}{1 + e^{-d \frac{|\mathbf{r}_{i,0} - \mathbf{r}_{j,L}|}{R_{ij}^{-1}}}} \quad (2.23)$$

which goes from 0 to 1 as the relative distance of $|\mathbf{r}_{i,0} - \mathbf{r}_{j,L}|$ between atom pairs is increasing.

For each pair of atoms separated by a distance, the dispersion correction essentially just adds an additional attractive potential to the result of DFT electronic structure computation. R_{ij} are referred to as van der Waals radii in Eq. 2.23. They make up the set of fittable parameters that constitute DFT+D a semiempirical correction technique, along with the fall-off scaled, the global scaling-factor s_6 , and the dispersion coefficients C_{ij} . Using a certain functional, these quantities are modified to provide results that are applicable to the real world. This has led to the construction of several parametrizations that are compatible with various exchange-correlation functionals.

A version created by Stefan Grimme et al. in 2004 that was designed to work with PBE functionals has so far proven to be highly reliable [64]. Grimme presented an updated parametrization termed DFT+D2 in 2007[65], and another one, DFT+D3 [66], in 2007 that even accounts for interactions between triplets of atoms to accurately describe three-body effects.

Following the completion of self-consistency cycle, dispersion corrections are only applied to the Kohn-Sham total energy. The wave functions or any other atomic or molecular properties are thus not immediately impacted. However, the forces operating on atoms in a specific configuration are determined by the gradient of the spatial energy landscape. The forces operating between atoms are changed when the dispersion correction is taken into account because it changes this landscape. This means that geometry relaxations, including lattice constant, cell volume, and shape optimizations, will vary depending on whether it is calculated with or without dispersion corrections. Figure 2.1 shows a calculation flowchart, in which this process is known as self-consistent field (SCF) calculations.

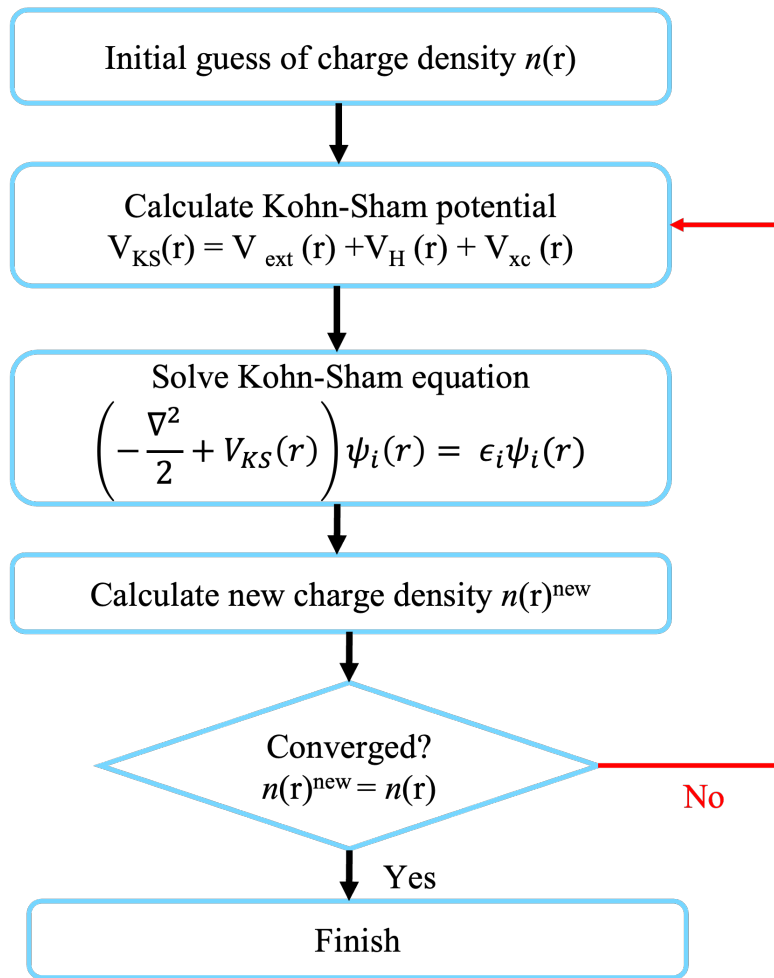


Figure 2.1: DFT-based calculation flowchart for the self-consistent field, beginning from setting initial charge density, $n(r)$ and the convergency will be acquired when $n(r)$ equals $n(r)^{new}$.

Chapter 3

Graphene and other two-dimensional materials

3.1 Introduction

3.1.1 Graphene

Since its discovery by Andrei Geim and Kostya Novoselov in 2004, graphene has become the subject of most interest in the field of current research[1]. Since then research on other 2D materials in this field has attracted increasing attention. Graphene, a stable two-dimensional (2D) material with a honeycomb structure [1, 2], has attracted significant attention both in experimental and theoretical studies for decades[3]. Graphene has excellent properties in ultra-high intrinsic mobility and large electrical conductivity[67], making graphene have many potential applications in electronic devices, transparent electrodes, and spintronics devices[2, 68].

3.1.2 Germanene

Although research on graphene and its ribbons is rapidly accelerating, some have begun to wonder whether group IV elements like germanene, have a stable honeycomb structure. Germanene, a 2D material derived from Germanium, is one of the fascinating materials to investigate. Due to its similarity to graphene, but differing from graphene, which is planar, germanene's most stable system is the low buckled system, making it an intriguing material to research. As germanium has larger atomic number compared to carbon, this materials have a much stronger SOC. The spin-orbit

coupling will increase by orders of magnitude with a small buckling[69]. According to study conducted thus far, germanene is semimetallic, has crossed energy bands at the Fermi level, and resembles graphene in that it has a dirac point at the k-point in the Brillouin zone [70].

3.1.3 TMD materials

TMDs are layered materials in which each unit (MX_2) is made up of two atomic layers of chalcogen (X) sandwiched between a transition metal (M) layer[71]. TMD materials are a class of 2D materials that have gained significant attention in the scientific community due to their unique electronic, optical, and mechanical properties[71]. Unlike traditional semiconductors, TMDs have a direct bandgap, which makes them promising candidates for next-generation optoelectronic devices[72]. TMDs are similar to graphene in strength and mechanical flexibility and provide excellent electrical transport as MoS_2 is found to have extremely high Young's modulus[73]. Those properties making them suitable for various applications in developing novel electronic devices[71].

3.2 Calculation Model

We utilized DFT to calculate SCF of graphene, germanene, MoS_2 , MoSe_2 , and MoTe_2 . FLAPW method is used to calculate graphene, MoS_2 , MoSe_2 , and MoTe_2 and germanene was calculated by using PHASE package. Exchange correlation of GGA is employed to all system. The muffin-tin radii of 2.6 Bohr for Mo, 1.9 Bohr for S, Se, and Te, and 1.2 Bohr for C were used. The convergence is set to 0.001 htr/bohr. Fourier expansion to charge density (G) of 9.8 a.u^{-1} . The cutoff energy for the plane-wave basis was set to 2.06 \AA^{-1} , and a 15×15 k-point mesh was used for self-consistent field (SCF) calculations with SOC. All the heterostructures were fully optimized by atomic force calculations.

3.3 Structure of 2D materials

Monolayer graphene has a honeycomb structure as shown in Fig. 3.1. We calculated optimized lattice constant of graphene, which is 2.45 \AA and is an agreement with the previous works [74, 75, 76]. Graphene's structure is a planar structure with a bondlength between Carbon atoms of 1.44 \AA .

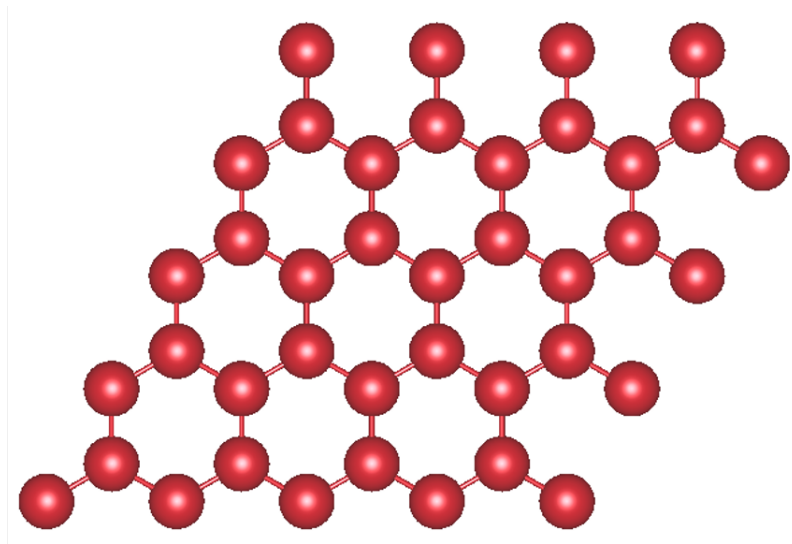


Figure 3.1: The structure of monolayer graphene

Germanene has a similar structure with graphene but a bigger lattice constant of 4.0 \AA as shown in the Fig. 3.2. But instead of having planar structure, germanene has a low buckled configuration of 0.7 \AA as shown in Fig.3.3 which is similar to that of silicene. These results are in good agreement with previous work [15]. The bondlength between atoms in pristine germanene is 2.44 \AA , which agrees with that of the previous study [77].

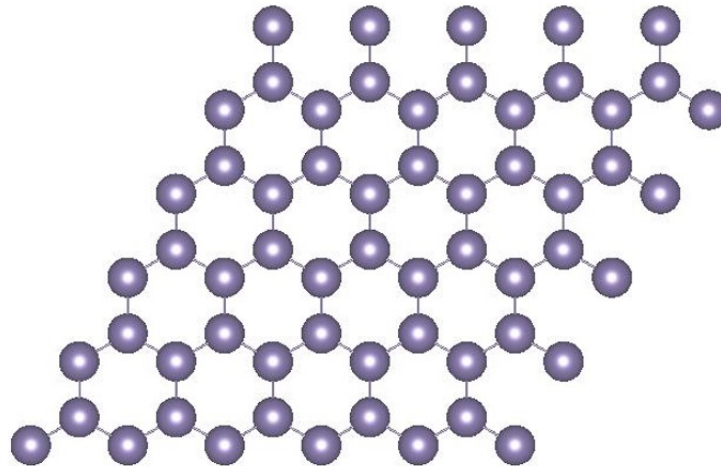


Figure 3.2: Supercell of germanene

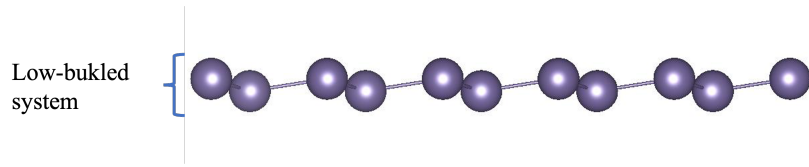


Figure 3.3: Low-buckled system of germanene

MoS₂ is made up of layers with a three-atom thickness of S-Mo-S. Adjacent layers of MoS₂ are connected by weak Van der Waals forces. In the Fig.3.4, blue and yellow colored atom represent Mo and S atom respectively. The optimized MoS₂ has a lattice constant of 3.15 Å while the bond length between Mo-S atom and S-S atom are 2.4 and 3.11 Å. These results correspond to the previous research[78].

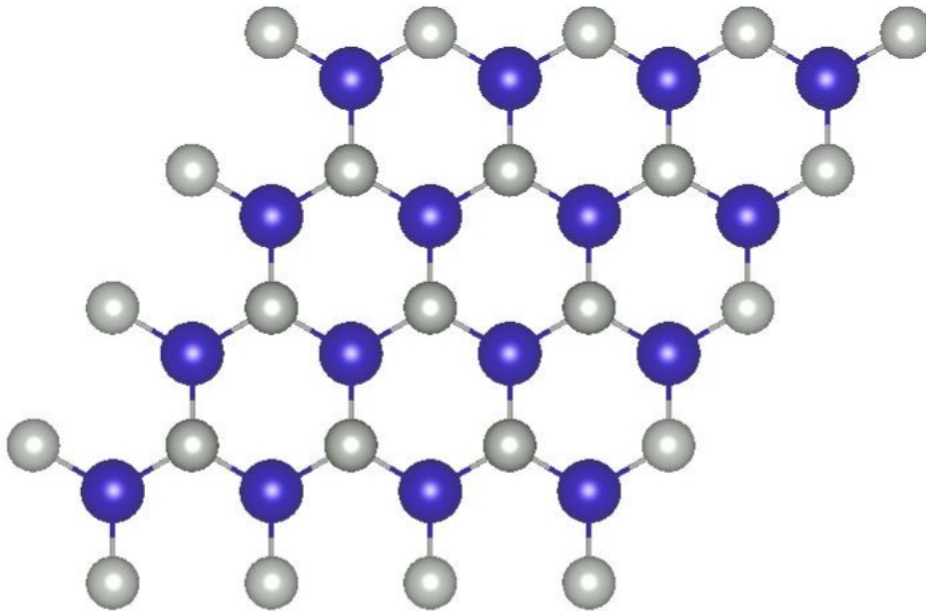


Figure 3.4: Top view of monolayer MoS₂ where blue and silver colored atoms represent Mo and S atom respectively.

As for MoSe₂ structure, MoSe₂ is a kind of layered material and characterized by the MX₂ formula of general TMDs, in which M and X represent Mo and Se, respectively. Mo and Se atoms bond with each other by covalent bonds and form basic layer of Se-Mo-Se [79]. Se-Mo-Se layers stack on one another and are connected via Van der Waals interaction, same as MoS₂. The bond length between Mo-Se atom is 2.5Å which in agreement with previous study[80]. Blue and green colored atoms from Fig. 3.5 illustrated Mo and Se atoms respectively.

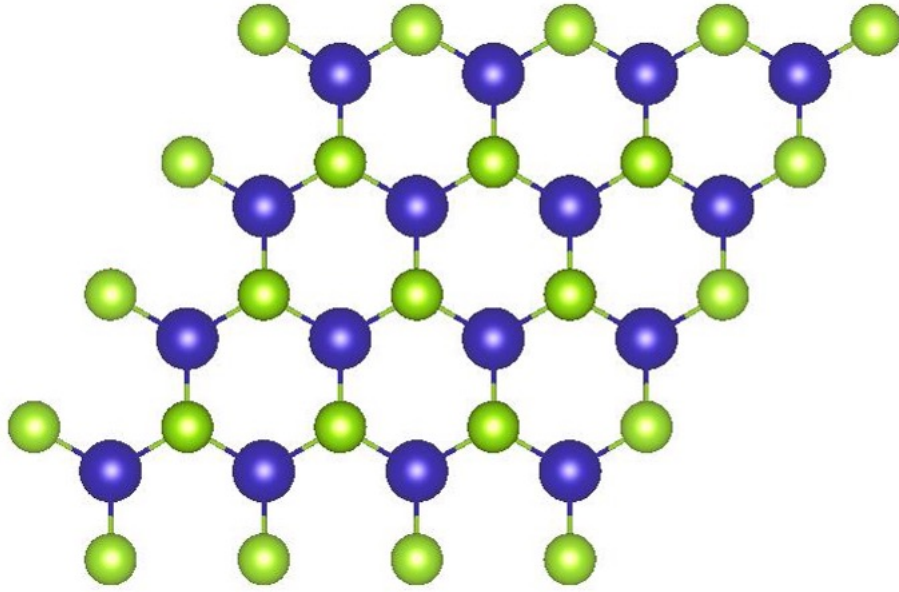


Figure 3.5: Top view of monolayer MoSe₂ where blue and green colored atoms represent Mo and Se atom respectively.

On the other hand, MoTe₂ has a very similar structure as MoS₂ and MoSe₂ represented by blue and gold colored atoms for Mo and Te atoms respectively in the Fig.3.6. The lattice constants for this structure was predicted to be 3.5 Å and the The Mo–Te bond length was also calculated to be 2.731 Å. These results are close to the previous study [81].

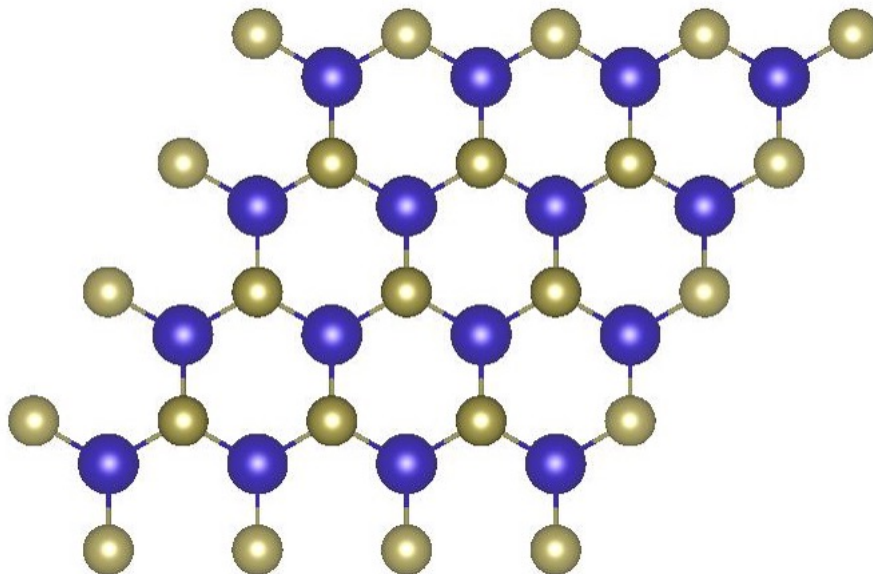


Figure 3.6: Top view of monolayer MoTe₂ where blue and gold colored atoms represent Mo and Te atom respectively.

3.4 Electronic structure

The electronic structures of graphene, MoS₂, MoSe₂, and MoTe₂ are shown in Fig. 3.7. From the calculations, a direct bandgap of 1.8, 1.5, and 1.1 eV had formed from MoS₂, MoSe₂, and MoTe₂ band structure respectively. These results are in agreement with previous studies[82, 71].

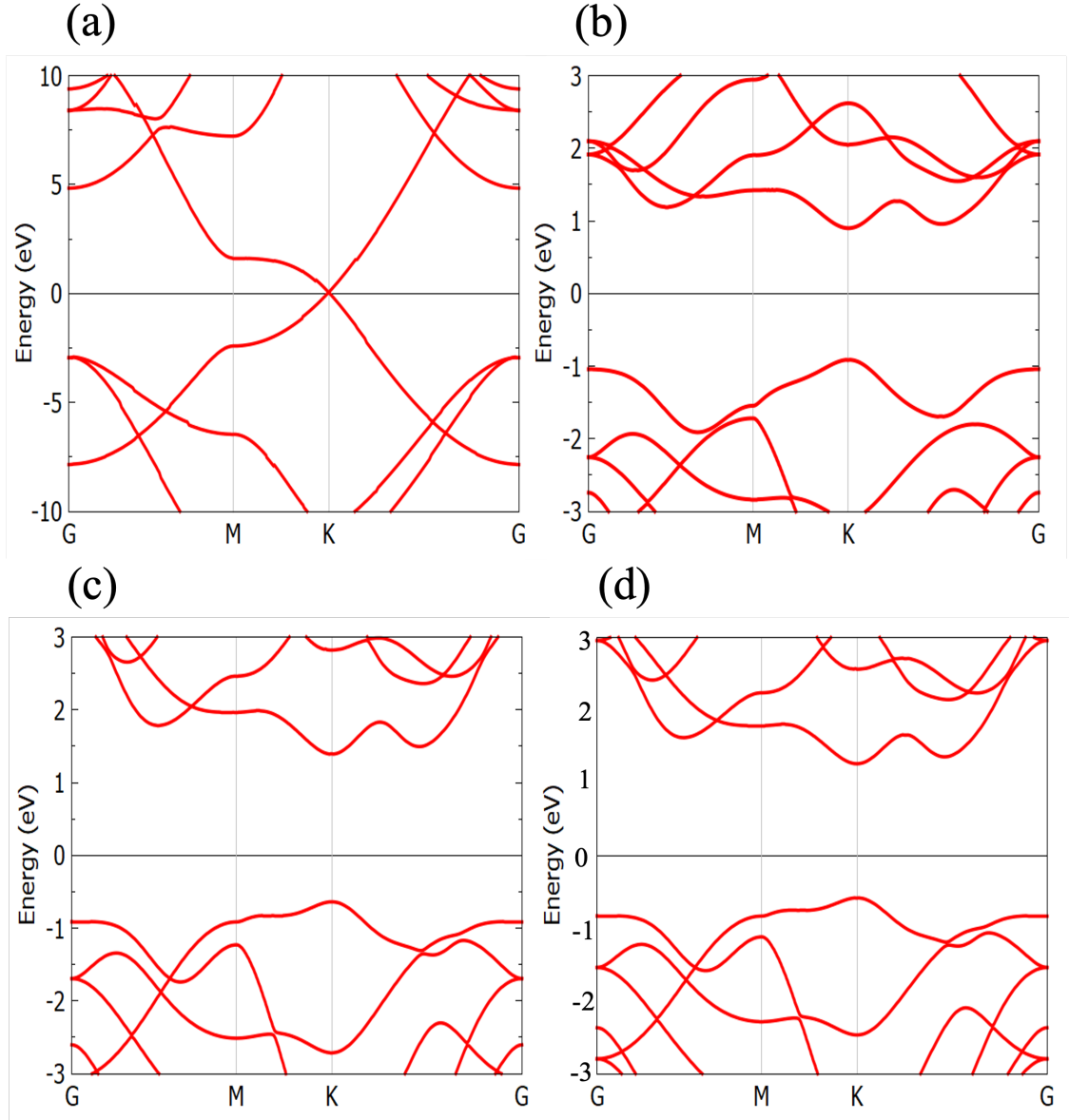


Figure 3.7: Band structure of (a) graphene, (b) MoS₂, (c) MoSe₂, and (d) MoTe₂.

3.5 Vacancy

To investigate the defected-structure of graphene and germanene, we firstly calculated monovacancy in monolayer graphene and monolayer germanene as shown in

Fig.3.8. One atom is removed from both pristine configurations of graphene and germanene at the center of. To estimate the energy required for the monovacancy system to form, we calculated formation energy as

$$E_f = \frac{1}{n}(E_d - \frac{N-n}{N}E_p) \quad (3.1)$$

where E_d , E_p , N , n are the total energy of the defective system, total energy of pristine, the number of atoms in the supercell, and the number of vacancies, respectively.

As a result, monovacancy graphene has a formation energy of 7.5 eV and in agreement with previous study [83]. This result is much larger than the formation energy of monovacancy germanene of 2.03 eV. Germanene has lower formation energy due to the low buckling system which requires less energy to be stable.

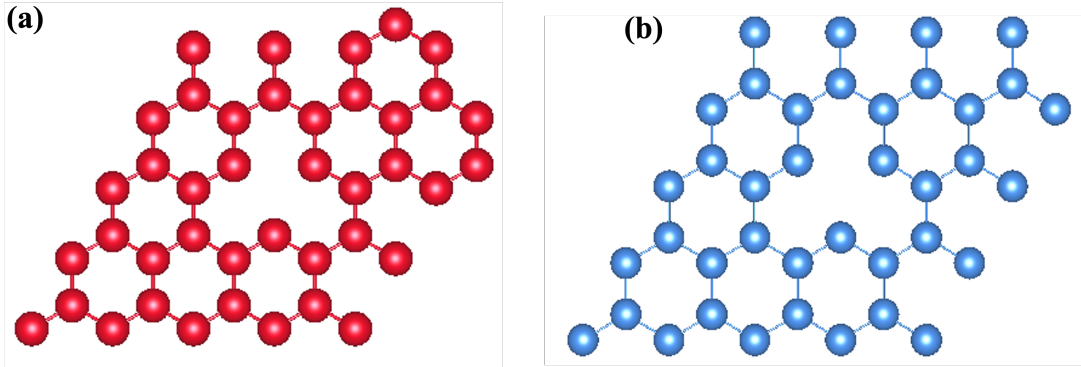


Figure 3.8: Monovacancy in monolayer (a) graphene and (b) germanene

We extended this study to multivacancy germanene by forming up to octavacancy configuration. The vacancy calculation is performed by removing up to 8 atoms and calculating the formation energy and dissociation energy.

The calculated formation energy (2.03 eV) of the monovacancy germanene is close to that in the previous studies (1.81 [84]). As for the divacancy, we find a 5-8-5 structure, which is in agreement with the result in Refs. [84]. The 5-8-5 structure was also found in graphene [85], silicene[86] and h-BN divacancies[87] as a stable configuration. The energy difference between the ideal and relaxed geometries (relaxation energy) of the mono- and divacancies are 0.42 and 1.55 eV, respectively. During The formation energy difference between divacancy and two monovacancies is 1.52 eV, thus, the divacancy is relatively very stable than the monovacancy. This result is similar in the case of graphene divacancy [85].

In the case of multivacancies, we simulate V2–V8 (Fig. 3.9) and Fig. 3.10. There are other possible initial configurations for each system of multivacancies. If the calculation is carried out accurately, any initial configuration will produce one stable configuration, which is the ground state. In this calculations, we use a large supercell consisting of 72 atomic-sites.

The calculated formation energies are given in Table 3.1. Atomic relaxation in trivacancy decreases the number of dangling bond (Fig. 3.10(a)) from five dangling bonds to only one dangling bond producing two pentagons in the relaxed structure. The bondlength of pentagon are identical, which is 2.83 Å (Fig. 3.10(a)). The relaxation energy is somewhat larger (1.68 eV) than that in the divacancy.

Atoms in the tetravacancy having six dangling bonds are relaxed with the energy of 0.89 eV. In the final relaxation, the dangling bonds decreases to two dangling bonds. This optimized structure produces two pentagons (Fig. 3.10(b)) with the bondlengths of 3.04 Å. The distance between two atoms having dangling bond is 3.90 Å, which is too far compared to the ideal bondlength (2.44 Å), thus, they are unbounded (Fig. 3.10(b)).

In the pentavacancy, seven dangling bonds of the unrelaxed structure decrease to three dangling bonds as effect of the relaxation with energy of 0.99 eV. We find two weak-bond pentagons with bondlengths of 3.53 Å, which are larger than those in the tri- and tetravacancies. The distance between two unbounded atoms (Fig. 3.10(c)) are 4.09 Å. Dangling bonds in relaxed structures of hexa-, hepta-, and octava- cancies remain as in the initial structures, which are six, seven, and eight dangling bonds, respectively. Inward relaxation occurs in these three configurations with relaxation energies of 0.69, 1.48, 1.57 eV, respectively. In the heptavacancy, there is one unbounded pentagon with the length of 3.97Å(Fig. 3.10(e)) while the octavacancy has two unbounded pentagons (Fig. 3.10(f)) with length of 3.67 Å. Comparing to the ideal bondlength, these lengths are too large causing the pentagons are unbounded.

We also analyze symmetries of the multivacancies. The tri-, tetra-, penta-, hepta-, and octavacancies have a C_{2v} symmetry since they are symmetric under C_2 through principle axis (Fig. 3.10(a–c)(e)(f)). Meanwhile, the hexavacancy belongs to a D_{6h} symmetry since it has C_6 , C_3 , C_2 , δ_h , δ_v , and δ_d (dihedral mirror) as well as the inversion symmetry (Fig. 3.10(d)).

We next calculate dissociation energies to analyze the stability of the multivacancies. Dissociation energy E_d represents the difficulty of vacancies to dissociate[85], it means

the larger the dissociation energy, the more stable the system. Dissociation energy data is provided in Table 3.1. From the table, we can assume that even numbers of vacancy (V2, V4, V6, and V8) have greater dissociation energy than of odd numbers of vacancy (V1, V3, V5, and V7) which indicates the stability of the system.

Table 3.1: Formation energies E_f and the dissociation energies E_d (in eV) of the V1 to V8.

Vacancy	E_f	E_d
V_1	2.03	1.09
V_2	2.54	1.46
V_3	5.46	0.87
V_4	6.03	1.15
V_5	6.75	0.87
V_6	6.76	1.24
V_7	8.17	0.27
V_8	9.00	1.32

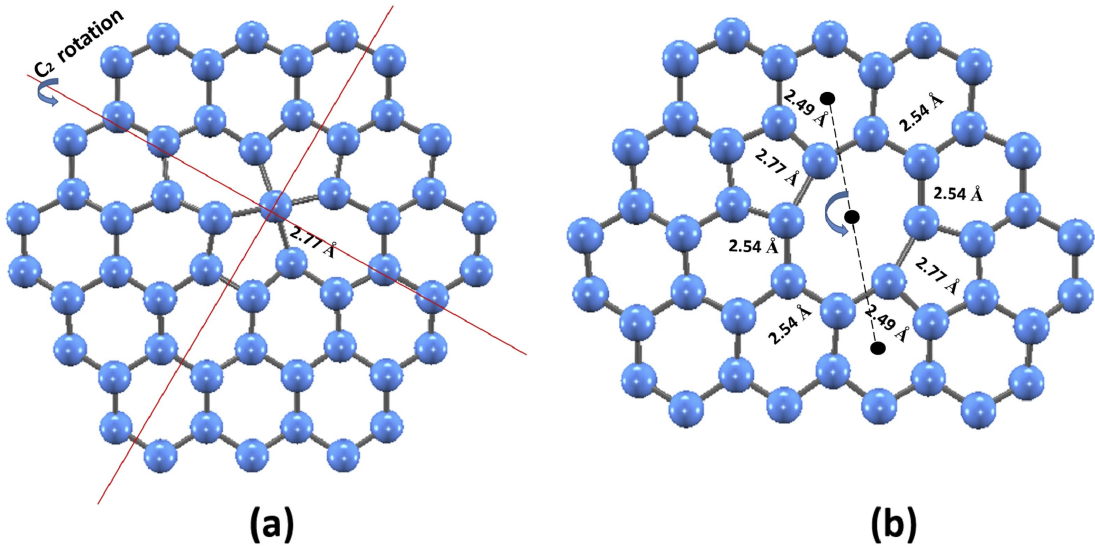


Figure 3.9: Relaxed structure of germanene (a) monovacancy and (b) divacancy

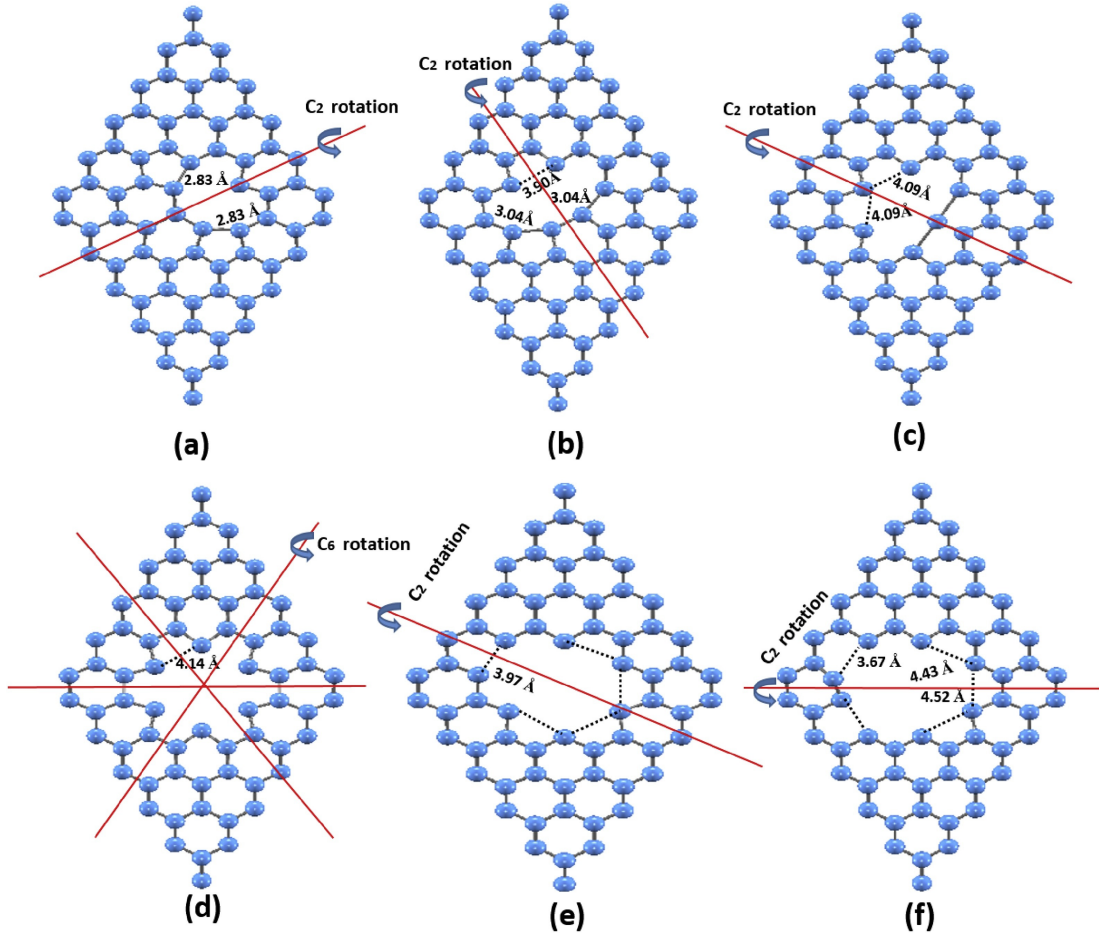


Figure 3.10: Relaxed structure of germanene (a) tri- (b) tetra-, (c) penta-, (d) hexa-, (e) hepta-, and (f) octavacancy.

In summary, we conclude the stable configurations of germanene multivacancies are V2, V4, V6, and V8. We propose that magic numbers are $2n$ ($n = 1, 2, 3, \dots$).

3.6 Concluding Remarks

In order to gain better understanding of the properties graphene, germanene, MoS_2 , MoSe_2 , and MoTe_2 , we carried out an investigation into their structural characteristics. Specifically, we focused on analyzing the presence of monovacancies in monolayer graphene and monolayer germanene. The calculations demonstrated that monovacancy germanene exhibits a lower formation energy compared to monovacancy graphene, primarily due to the low buckling in germanene. Additionally, we conducted an extended study on multivacancy germanene and its structural stability. Through the analysis, we discovered that the most stable multivacancy structures in germanene were those with an even number of vacancies. The identified appropriate structures from this

study will be used for further calculations and investigations in the next chapter.

Chapter 4

Lithium intercalation in bilayer graphene

4.1 Introduction

Due to its high energy density, renewable resources, and environmental friendliness, lithium ion batteries (LIB) have been extensively used in portable electronic devices. The development of novel electrode and electrolyte materials for lithium ion batteries has thus received a lot of attention. A sensible choice of anode material is somewhat essential for improved efficiency. Despite significant research efforts to discover alternatives, carbon is still the only anode material for lithium ion batteries that is currently considered commercially viable[88].

Graphite is currently a popular anode material for lithium ion batteries, despite the fact that its low Li storage capacity (372 mAh/g) [89] prevents it from meeting the demand for big power batteries in electric vehicles. Following the discovery and popularity of graphene, some studies on its usage as potential anode material for lithium ion battery have been done. Numerous previous works reported that graphene-modified electrode materials could enhanced energy-storage performances[30]. Useful properties of graphene such as high mechanical flexibility, high specific surface area, ultra-thinness, good electrical conductivity, and high theoretical capacitance can be used for energy storage technology[90].

Bilayer graphene with lithium is a promising material for the future of battery technology. Graphene, a thin layer of carbon atoms, is known for its excellent mechanical, thermal, and electrical properties. Bilayer graphene, which consists of two layers of

graphene stacked on top of each other, has even more remarkable properties. The addition of lithium to bilayer graphene enhances its conductivity, making it an ideal candidate for use in batteries. Bilayer graphene was shown to exhibit multilayer lithium storage with a hexagonal close packing, far exceeding the capacity of graphite[91].

Recently, many prior studies reported that defect engineering is one of possible ways to tune electronic properties of materials including to enhance the capacity of bilayer graphene. Defect engineering that can be easily introduce is vacancy defect (point defect). Previous study concluded that by removing one or more C atom from the bilayer graphene, the capacity of lithium that can be inserted is increased significantly[92, 88].

Here, we have introduced point defects into bilayer graphene and studied their stability and lithium storage capacity using density functional theory (DFT)-based calculations. The highest lithium intercalation was achieved by applying external electric field.

4.2 Calculation Model

We performed first-principles calculations using Full-potential linearized augmented plane-wave method (FLAPW) method[63]. Exchange correlation of generalized gradient approximation was employed [93]. Muffin-tin (MT) sphere radii of 1.2 Bohr for C was used. The cutoff energy of plane-wave basis was set to 3.9 Bohr⁻¹, and a 5 × 5 *k*-point mesh was used for the entire calculations. All atomic positions were fully optimized by atomic force calculations. As for the configuration, we use 3 × 3 of supercell graphene and we stack two layers of graphene sheets with AA and AB stacking method consists of 18 atoms of each layer which makes 36 atoms in total as illustrated in Fig. 4.1(a) and (b). Additionally, a homogenous external electric field up to ±0.5 V/Å was applied along the *z*-axis, i.e., perpendicular to the surface plane as illustrated in Fig. 4.1(d).

To conduct a thorough investigation of the behavior of Li adsorption between bilayer graphene, we compare the stability of different configuration and different position of lithium by calculating adsorption energy. We define the adsorption energy (E_{ad}) of Li in the bilayer graphene by using the equation[94]:

$$E_{ad} = E_{V+Li} - E_V - E_{Li} \quad (4.1)$$

where E_{V+Li} and E_V represent the total energies of the the vacancy structure with and without Li, respectively. E_{Li} defines the energy per atom for the bulk lithium.

Intercalation energy of the system is defined by[92]:

$$E_{intercalation} = \frac{1}{n}[E_{V+Li} - E_V - nE(Li)] \quad (4.2)$$

where $E_{intercalation}$ is intercalation energy, n , and $nE(Li)$ represent number of lithium and energy of bulk lithium, respectively.

For the energetically advantageous structure, the intercalation energy parameter must be negative, indicating that the final structure is more stable than the structure that does not involve intercalation[92]. The lower intercalation energy the more we can insert lithium inside the system which results in increasing capacity of lithium.

4.3 Bilayer graphene structure stability

We start off by explaining the stacking structures of bilayer graphene. Bilayer graphene demonstrates the AB stacking structure, according to Ferrari et al.'s discovery[95]. Liu et al. noted the existence of bilayer graphene in conjunction with AA stacking[96]. We create the bilayer graphene structures depicted in Fig. 4.1(a-b) based on the various arguments mentioned above to investigate the stability of the stacking to use in the further calculations.

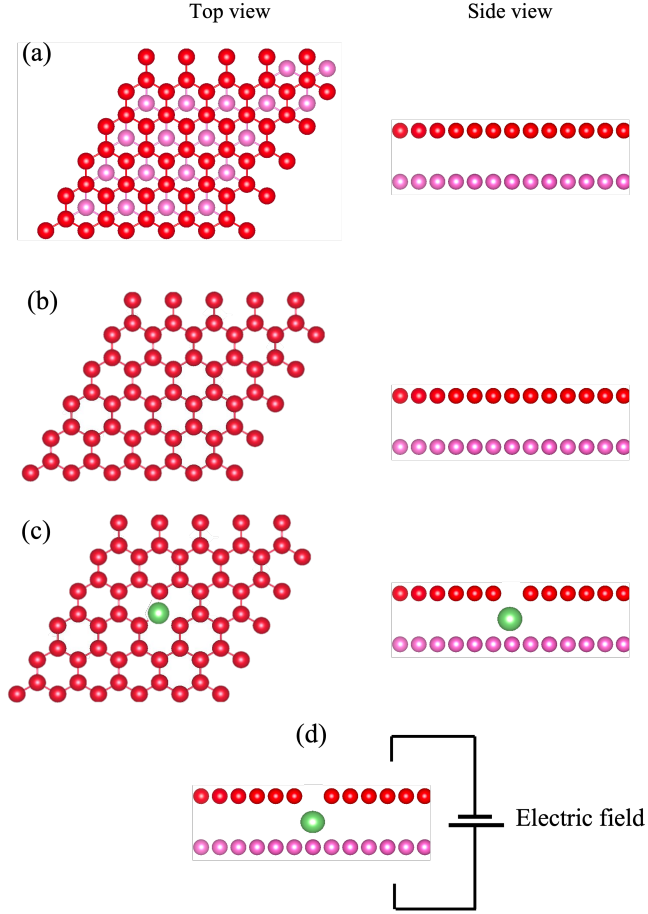


Figure 4.1: Graphene bilayer structure of (a) top and side view of AB stacking, (b) top and side view AA stacking, (c) top and side view of lithium inserted into defected bilayer graphene, and (d) the arrangement of external electric field applied perpendicularly to the system. Red and Pink-colored atoms represent the top and bottom layer of the bilayer configuration, respectively. In AB stacking half of carbon atoms in the bottom layer are located at the hollow site of top layer while in AA configuration, top and bottom layers are perfectly aligned.

We then calculated the binding energy of both stacking and found that AB stacking is more stable proven by lower of binding energy of 0.015 eV/atom compared with AA stacking. This result is in agreement with previous study[92]. The observed difference can be attributed to the contrasting binding energies required for the two stacking arrangements. Specifically, in the AA system, a larger binding energy is necessary when all carbon (C) atoms are positioned on top or bottom of each other. Conversely, in the AB configuration, only half of the C atoms are situated within the hollow spaces of the adjacent layer.

After calculating AA and AB stacking for pristine structure, we further investigate

the stability of AA and AB stacking in vacancy system. By comparing the total energy of both stacking, we found that AA stacking graphene is more stable than AB stacking by 0.014 eV/atom in a vacancy system. By acquiring this result, we conclude that AA stacking system is more reliable to use for further investigation. A previous study also mentioned that when the number lithium inside the bilayer graphene increases, the configuration of bilayer graphene with AB stacking will evolve into with AA stacking-shape. Therefore, the vacancy bilayer graphene with AA stacking is chosen for the following investigation[88, 92].

To study the effect of vacancy at the molecular level, the band structures and density of states (DOS) of AA and AB stacking for pristine and vacancy configurations were calculated and shown in Fig. 2. In the Fig. 4.2(a) and (b), it is indicated that it has Dirac cone in the band structure at the high symmetry point of K. At K, the valence and conduction bands are touching. In the band structure analysis of vacancy configurations (second row of Fig. 4.2), the presence of additional bands near the Fermi level can be attributed to the imbalance of electrostatic potential between the two graphene layers. The occurrence of a vacancy defect in the top layer disrupts the uniformity of the electrostatic potential. Consequently, there is a redistribution of electrons in response to this disruption, resulting in the emergence of new electronic states and the formation of additional bands within the energy spectrum [97]. This phenomenon can be understood as the response of the electronic structure to the localized perturbation introduced by the vacancy defect.

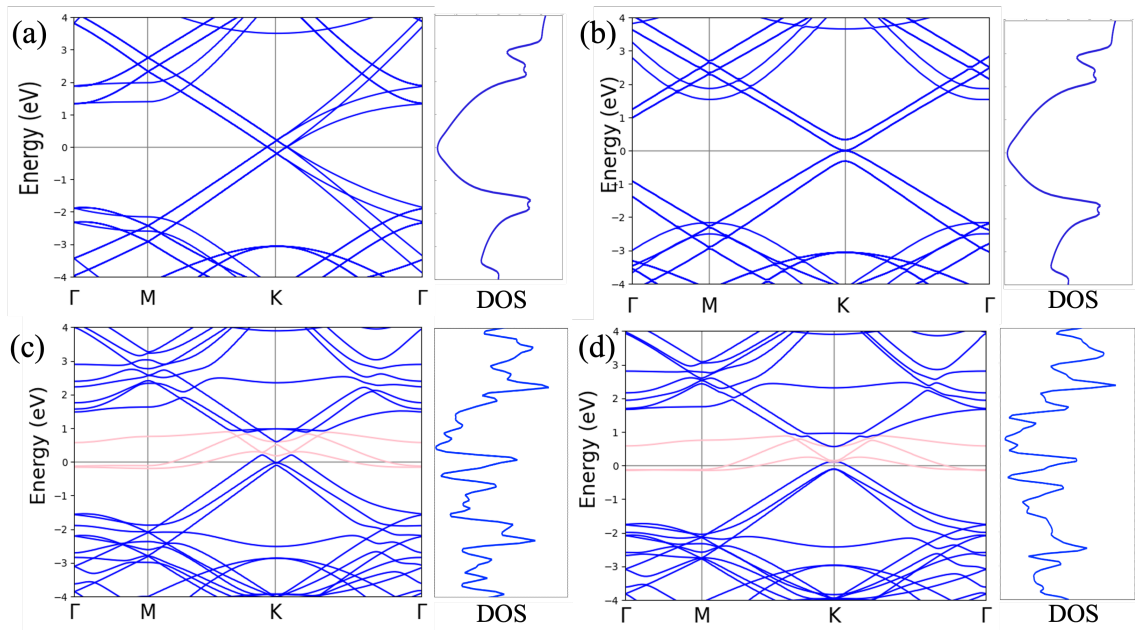


Figure 4.2: Band structure and DOS of (a) pristine AA stacking, (b) pristine AB stacking, (c) defected AA stacking, and (d) defected AB stacking. Additional bands emerged at fermi level in vacancy structures are represented by pink colored bands.

We then investigate the behavior of Li adsorption in bilayer graphene. We determined the adsorption energy of Li in bilayer graphene to compare the stability of these sites, using the equation Eq. 4.1. $P4$ of the figure represents the vacancy site of the bilayer graphene. The result of the adsorption energy of each position is shown in Fig. 4.3(a). As a parameter, a negative value of adsorption energy indicates that Li can adsorb stably and spread out on the surface. Lower adsorption energy values indicate more stable adsorption sites[94]. In the result in Fig. 4.3(a), all values of adsorption energy were negative, indicating that Li can stably adsorb and spread out at these sites. Notably, adsorption energy values were lower when Li was located at a vacancy defect and became higher as it moved away from the defect. From the Fig. 4.3(a), we assumed that $P4$ is the most preferred position to insert lithium because of this position acquires the lowest adsorption energy of 1.96 eV. This result is close to lithium adsorption in the Stone-Wales defected-bilayer graphene of 2.17 eV [98]. The furthest position of $P6$ acquires the highest adsorption energy of -0.38 eV and gradually become more negative as the position is getting closer to the vacancy site as corresponds to previous study which mentioned that as Li gets closer to the vacancy defects, its adsorption energy gets more negative which makes the position is more favorable. This is due to vacancy defects create dangling bonds, which attract electrons to form new

chemical bonds with Li and increase its sticking ability [94]. We also found this result is much lower than adsorption of lithium in pristine bilayer graphene of -0.19 eV and in agreement with a study of defected monolayer graphene [99].

To increase the stability of the system, we modify the external electric field applied to the defected bilayer graphene with lithium inserted at the most favorable position ($P4$) as default position. The result of adsorption energy for different external electric field is shown in Fig.4.3(b). From this figure, both positive and negative electric field modulate the adsorption energy. Furthermore, positive external electric field decreases adsorption energy more than negative external electric field with the same magnitude. The lowest adsorption energy of -2.3 eV is emerged from external electric field of 0.5 V/Å, with 0.35 eV difference with the system without external electric field. For the same magnitude in negative value, the adsorption energy obtained is -2.07 eV, 0.23 eV higher than in positive value. The positive electric field direction, which propagates from the top layer where the defect site is located towards the bottom layer, is the cause of this phenomenon. This increased electron polarization around the defect site is caused by the directional electric field, which enhances adsorption. This charge redistribution can affect the adsorption energy of the lithium atoms on the graphene surface [100, 101].

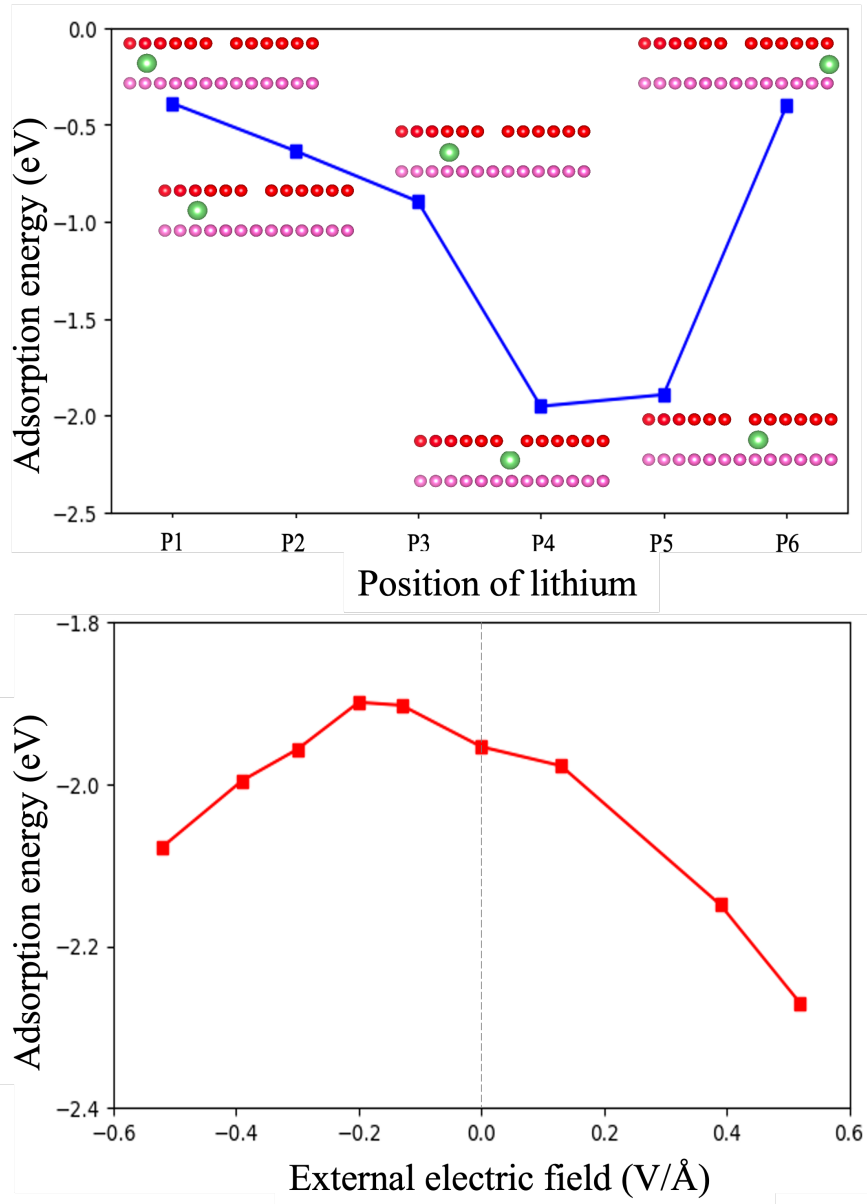


Figure 4.3: Adsorption energy in function of (a) position of lithium and (b) external electric field. The insets in (a) illustrate the position of lithium inserted into the bilayer graphene correspond to P1 to P6, where P4 refers to the position of lithium exactly under the defect site and P6 represents the furthest position from the defect site.

In the case of Li adsorption in defected system, the presence of a dangling bond serves as a bridge for electron transfer between Li and graphene, improving their interaction i.e. adsorption[102]. When an electric field is applied, it exerts a force on the electrons, prompting them to move through the dangling bond. As a result, the electrons become more concentrated in the region, leading to a higher density shown in Fig.4.4. This increased electron density reinforces the attractive interaction between Li and graphene, further enhancing the adsorption process.

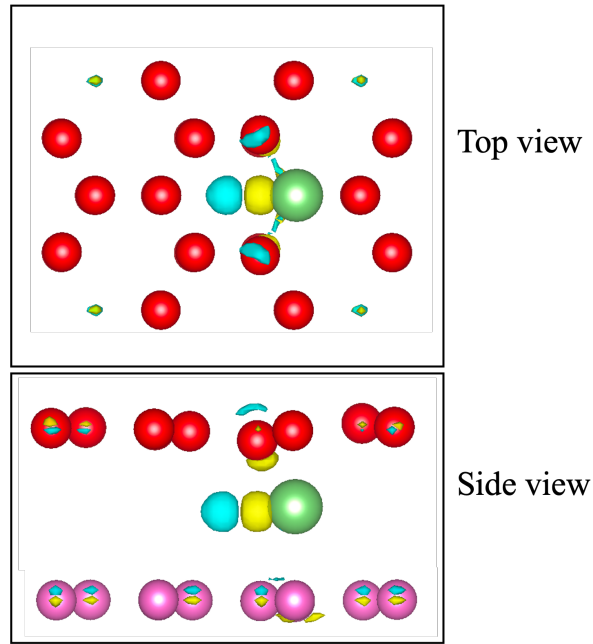


Figure 4.4: Charge density with lithium inserted into defected bilayer graphene.

4.4 Intercalation and capacity

To investigate the amount of energy required to insert a lithium atom between the two layers of graphene, we calculate intercalation energy. Intercalation is a term that describes the insertion of a guest molecule or atom into a host lattice, with minimal disturbance to the structure of the compound. This process can be reversed either chemically or thermally[103]. The model of lithium insertion between bilayer graphene is shown in Fig.1(c). A lower intercalation energy implies that less energy is required to insert the intercalating material, which can result in a more efficient and faster intercalation process.

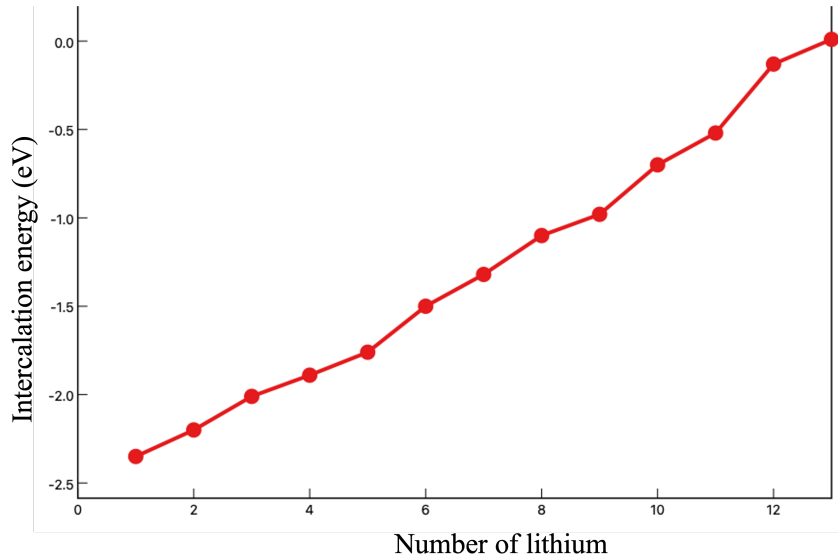


Figure 4.5: Intercalation energy in function of number of lithium atom inserted into the system. Zero is the threshold for the maximum amount of lithium atom can be accomodated into the system.

Figure 4.5 illustrates the intercalation energy as a function of the number of lithium atoms inserted into defected bilayer graphene under the influence of an external electric field. The zero energy level represents the threshold for accommodating lithium atoms in the system. The graph reveals that a higher energy is required to accommodate a larger number of lithium atoms. For instance, the intercalation energy for one lithium atom is determined to be -2.27 eV, while accommodating 12 lithium atoms necessitates an intercalation energy of -0.19 eV. Notably, when considering a larger number of lithium atoms (13 atoms), a positive intercalation energy is observed. Based on this observation, we conclude that 12 lithium atoms represent the maximum number that can be accommodated within the system. It is important to mention that in the pristine system, the maximum capacity for lithium atoms is limited to 5. However, with the introduction of defects and the application of an external electric field, the system undergoes an expansion of its capacity, allowing it to accommodate up to 12 atoms.

To futher investigate the capacity of the defected bilayer graphene under external electric field, theoretical capacity of bilayer graphene is defined by[104],

$$C = \frac{nF}{M_G + nM_{Li}} \quad (4.3)$$

where n is the number of Li atoms, F is the Faraday constant (26,801 mAh/mol), M_G is the molecular weights of bilayer graphene, and M_{Li} is the molecular weight of

lithium atom.

Table 4.1: Number of lithium atom that can be accommodated in the system (N_{Li}), composition of lithium atom per number of carbon atom (C_{Li}), and capacity of each structure.

Structure	N_{Li}	C_{Li} (%)	Capacity (mAhg ⁻¹)
Pristine	5	13.9	283
Defected with electric field	12	34	638

In the pristine system, the maximum capacity for accommodating lithium atoms is limited to 5 atoms, resulting in a theoretical capacity of approximately 283 mAhg⁻¹ or around 13.9% composition as stated in Table 4.1. However, when considering defected bilayer graphene with external electric field, the system can accommodate up to 12 lithium atoms, leading to an increased capacity of 638 mAhg⁻¹ (with composition of 34%) or approximately a 125% increase. Notably, this capacity enhancement demonstrates an almost twofold improvement compared to the current capacity of graphite, which stands at 372 mAhg⁻¹.

4.5 Concluding Remarks

The present research has focused on investigating the effect of an external electric field on the intercalation of lithium atoms in defected-bilayer graphene. Our results have demonstrated that the application of a larger external electric field can significantly enhance the intercalation of lithium attributed to the charge redistribution at defect site, leading to a higher capacity of the system up to 638 mAhg⁻¹ which almost double compared to current capacity of graphite of 372 mAhg⁻¹.

In conclusion, this study demonstrates the potential of bilayer graphene as a replacement for graphite in Li-ion batteries, offering enhanced intercalation of lithium with the use of an external electric field. Further research and development in this area can contribute to the advancement of more efficient and sustainable energy storage systems.

Chapter 5

Graphene-MoS₂heterostructure

5.1 Introduction

The low intrinsic spin-orbit coupling (SOC) strength in graphene further provides an advantage in spin transports [38]. However, the absence of bandgap in graphene limits graphene usage in electronics due to its poor on/off ratio [105]. Although many efforts on the bandgap opening have been carried out previously in various ways, such as doping [106, 107, 108], creating multilayer graphene [109], and constructing bilayer graphene that demonstrates an electrically gate-controlled, continuously tunable bandgap of up to 250 meV [110], applying an electric field [68], and forming heterostructures [105, 111, 112, 113, 114], the understanding of the electronic structure of graphene, e.g., focusing the bandgap opening, is crucial for making graphene applicable in a broader area.

Transition-metal dichalcogenide (TMD) is a desired group of materials due to their outstanding properties in potential utilization, such as for electronic devices, optoelectronic devices [115], gas sensing [21] and energy storage [22]. MoS₂, as a member of TMD, shows intriguing mechanical and electrical properties [116]. Unlike graphene, two-dimensional MoS₂ is an excellent semiconductor with a 1.8 eV bandgap. Meanwhile, the bulk system has a 1.2 eV indirect bandgap [117, 46]. It further notes that TMD possesses a strong intrinsic SOC of tens of meV compared to graphene [118]. A direct bandgap in two-dimensional MoS₂ could be a solution for bandgap opening on graphene and become the motivation to combine both materials as a heterostructure.

For years, keen interest has been given to heterostructure materials [113, 8, 119, 120, 121]. A number of the previous studies show exemplary implementations for a

heterostructure of graphene and TMD, for example, graphene-MoS₂, applied to supercapacitors, gas sensors, spintronic devices, and electrochemical detectors of Morin [122, 123]. Heterostructures of the others, graphene-MoSe₂ and graphene/WTe₂, are potential materials in the optoelectronic field [124, 125], graphene-MoTe₂ and graphene/WSe₂ are also beneficial in photodetector devices [119, 126], and graphene/WS₂ is a prospective material for nanoelectronics and optoelectronic devices [127, 128].

In the present work, we have systematically performed density functional theory (DFT) calculations to clarify the effects of the electronic structure of graphene-MoS₂ on stacking, element substitution, and interlayer distance. We find that stacking orientation is not significantly affecting the electronic structures, which contrasts with how element substitution and interlayer distance successfully tune the electronic structures. The findings are essential to navigating the tuning of electronic properties of graphene-MoS₂ heterostructure for further investigation.

5.2 Calculation Model

First-principles calculations using the full-potential linearized augmented plane-wave (FLAPW) method [62] that treats a single slab geometry were carried out to investigate the electronic structures of graphene-MoS₂[129]. Generalized gradient approximation (GGA) was employed as exchange-correlation[93], and to account for long-range dispersion correction, the DFT-D2 method was employed[130]. The core states were treated fully relativistically, and the valence states were treated semi-relativistically, where spin-orbit coupling was incorporated using the second variational method [63]. The muffin-tin radii of 2.6 Bohr for Mo, 1.9 Bohr for S, Se, and Te, and 1.2 Bohr for C were used. Fourier expansion to charge density (G) of 9.8 a.u⁻¹. The cutoff energy for the plane-wave basis was set to 2.06 Å⁻¹, and a 15×15 *k*-point mesh was used for self-consistent field (SCF) calculations with SOC. All the heterostructures were fully optimized by atomic force calculations.

As for models, graphene-MoS₂ heterostructures with two different later-stacking orientations, namely, C_S stacking for C atoms stacked on the top of S atoms and C_{Mo} stacking for C atoms stacked on the top of Mo atoms, as illustrated in Fig. 5.1. These stacking orientations were considered based on the previous study which analyzed the most stable stacking for bilayer MoS₂ [131]. The structural periodicity in graphene and MoS₂ layers sets with two ratios, 1:1 and 4:3, i.e., the 1:1 heterostructure con-

sists of 1×1 cell of both graphene and MoS_2 while the 4:3 heterostructure is 4×4 of graphene and 3×3 of MoS_2 . For the element substitution, then, three graphene/TMD heterostructures, consisting of graphene- MoS_2 , graphene- MoSe_2 , and graphene- MoTe_2 , respectively, were considered. Finally, the dependence of interlayer distance between graphene and MoS_2 in the heterostructure was analyzed by varying the distance from 2.6 to 3.6 Å.

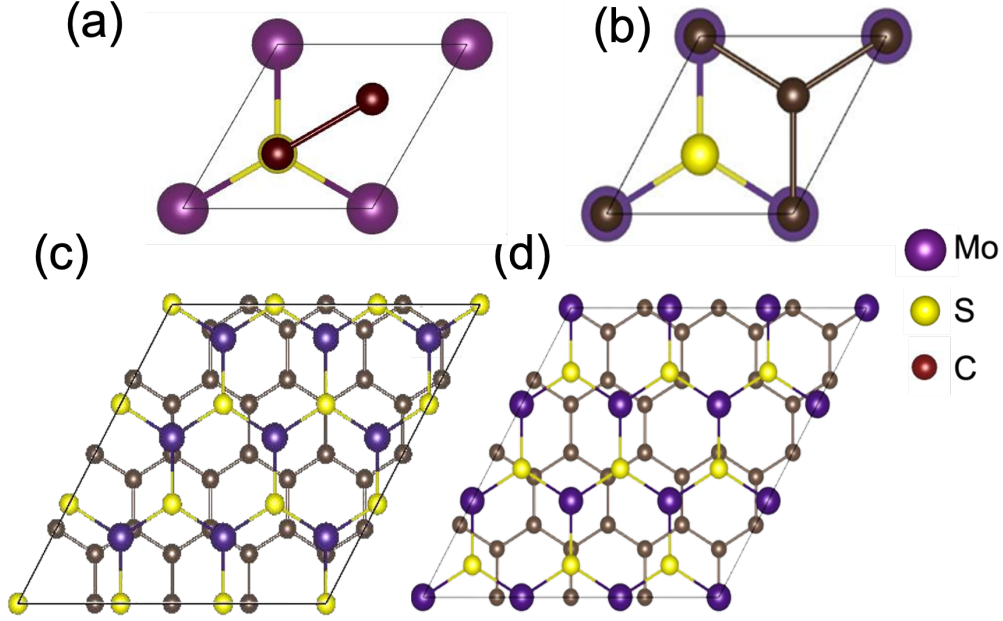


Figure 5.1: Calculated band structures of graphene- MoS_2 , graphene- MoSe_2 , and graphene- MoTe_2

5.3 Stacking orientation, element substitution, and interlayer distance effect on the electronic structures

5.3.1 Stacking orientation

We first confirmed that the calculated lattice constants of single monolayers of graphene and MoS_2 are 3.16 and 2.46 Å, respectively, which agree with the previous works [132] Fig. 5.1 displays the optimized 1:1 and 4:3 heterostructures of graphene- MoS_2 for the C_S and C_{M_0} stackings. In the 1:1 heterostructure, for both C_S and C_{M_0} stackings, the bond lengths of C-C in the graphene layer and Mo-Mo atoms in the MoS_2 layer are 1.73 and 3.09 Å, respectively, and the interlayer distances between

graphene and MoS₂ layers are 3.38 Å. Even in the 4:3 heterostructure, the interlayer distances in the C_S and C_{Mo} stackings are 4.47 and 3.50 Å, respectively, and the present results correspond to the previous works[133, 134] Despite the change in the stacking orientations, the structural properties remain the same.

Figure 5.2 shows the calculated band structures and densities of states (DOSs) of the 1:1 and 4:3 heterostructures in the C_S and C_{Mo} stackings. The identical feature of the Dirac cone in the band structures and DOSs can be seen in each heterostructure regardless of the stackings. The bandgap at K in both stackings is distinguishable, as shown in the figure where the bandgaps of the C_S and C_{Mo} stackings are 19 meV and 8.5 meV. The total energy in the C_{Mo} stacking for the 1:1 heterostructure is slightly lower than that in the C_S one by only 0.872 meV/cell. It occurs in the 4:3 heterostructure, where the total energy of C_{Mo} stacking is lower than that on the Cs by 0.54 meV/cell.

Charge density calculation is added to analyze the presence of charge transfer between layers in the heterostructure. Figure 5.3 shows the charge density plot for both C_{Mo} and C_S stacking orientation for optimized 1:1 structure. For both stacking orientations, it is shown that no charge is transferred from one layer to another.

The physical origin of the bandgap that emerged in the graphene-MoS₂ is due to the hybridization between the graphene and MoS₂ layers, where weak interaction bonds the layers, proven by no charge transfer between both layers. Thus, the stacking orientation does not affect their electronic structures qualitatively as both have identical band structure and does not change the character of the material. However, stacking orientation changes the band structure quantitatively as the band gap differs from each other. This result also corresponds to the previous study, which studied the 5:4 and 4:4 heterostructures [135].

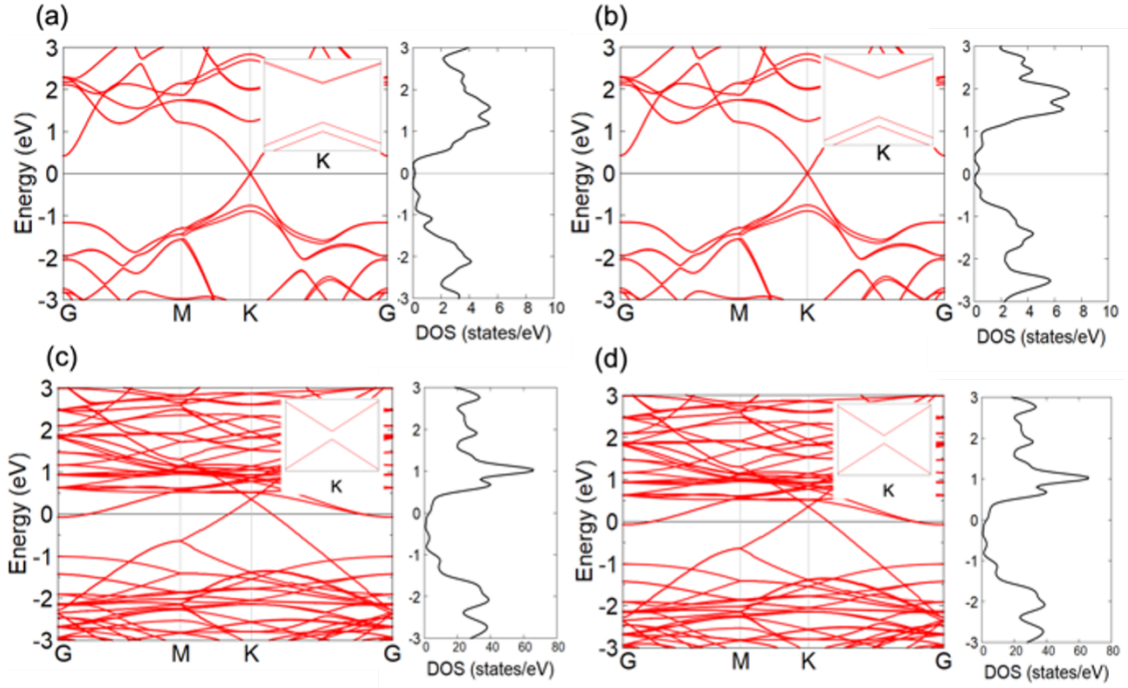


Figure 5.2: Band structures and DOSs of graphene-MoS₂ heterostructures under different structure arrangements: (a) 1:1 structure with C_S stacking orientation, (b) 1:1 heterostructure with C_{Mo} stacking orientation, (c) 4:3 structure with C_S stacking orientation, and (d) 4:3 structure with C_{Mo} stacking orientation. The insets show a bandgap at K in each structure

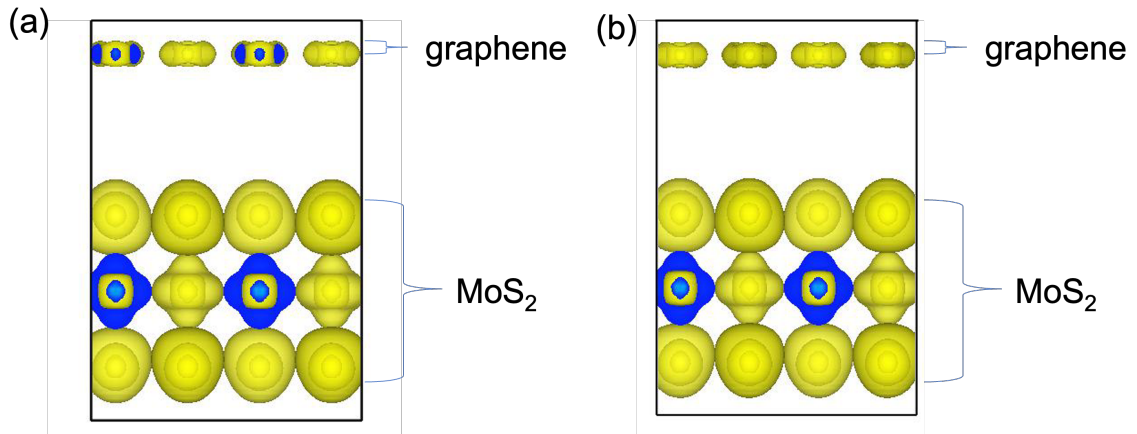


Figure 5.3: Charge density of 1:1 structure (a) C_{Mo} stacking orientation and (b) C_S stacking orientation. The yellow color shows positive charges

5.3.2 Dependence of element substitution

We next present the results for three different heterostructures, graphene-MoS₂, graphene-MoSe₂, and graphene-MoTe₂, to examine the effect of element substitution.

As for the graphene-MoS₂, we chose the C_{Mo} stacking with the lowest total energy. The calculated interlayer distances and bandgaps for the three heterostructures are given in Table 5.1, and the band structures are shown in Fig. 5.4. From the calculated band structures, we observe that the bandgap in the Dirac cone at K of each system varies in insignificant values. The graphene-MoTe₂ shows a metallic characteristic. Enlarged pictures along the G-M-K-G direction show that the Dirac cone for the graphene-MoTe₂ is shifting down towards the valence bands.

The calculated optimized interlayer distances for the three heterostructures are given in Table 5.1. The three heterostructures have different values of the optimized interlayer distances, where the graphene-MoS₂ has the greatest distance of 3.38 Å compared to those in the graphene-MoSe₂ (3.28 Å) and graphene-MoTe₂ (3.19 Å). Alongside the optimized interlayer distance, the calculated bandgaps located on the Dirac cone in graphene are also given in Table 5.1. Meanwhile, the heterostructure of graphene-MoS₂ has the lowest bandgap of 8.5 meV compared to graphene-MoSe₂ of 15 meV. These results show that element substitution in these graphene/TMD heterostructures affects the electronic structure of the system quantitatively and qualitatively as the bandgap shows different values as well as the change in the valence and conduction bands. Furthermore, the graphene-MoTe₂ demonstrates an exciting transformation from semiconductor to metal characteristics.

For further analysis, we calculated projected density of states (PDOS) as shown in Fig. 5.5. Based on these graphs, we can see that the orbital which has a significant contribution to valence and conduction band is *d* orbital which is represented by the green color. We also can spot the differences between each heterostructure from the states shown around the Dirac cone.

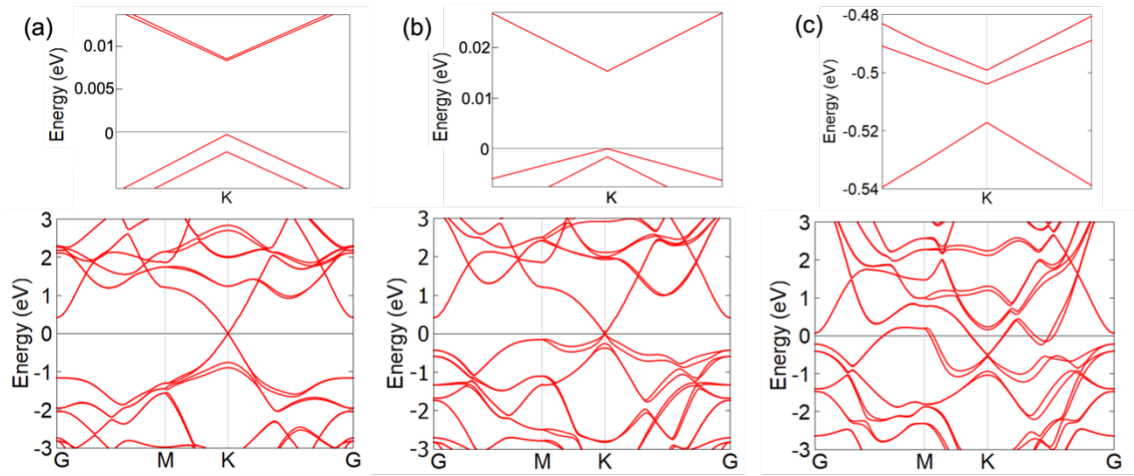


Figure 5.4: Calculated band structures of graphene-MoS₂, graphene-MoSe₂, and graphene-MoTe₂

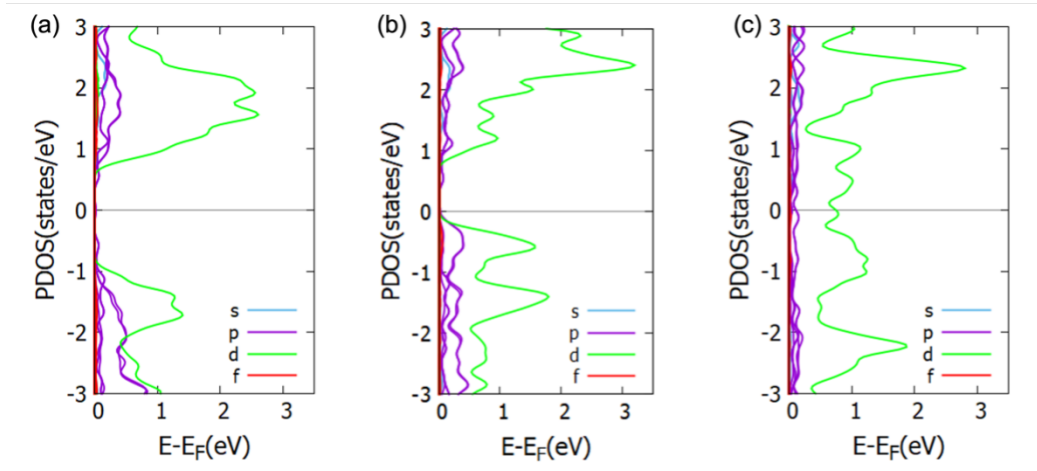


Figure 5.5: Calculated DOSs of graphene-MoS₂, graphene-MoSe₂, and graphene-MoTe₂

Table 5.1: Calculated interlayer distance (d) and bandgap ΔE of graphene-MoS₂ and graphene-MoSe₂

Elements	$d(\text{\AA})$	ΔE (meV)
graphene-MoS ₂	3.38	8.5
graphene-MoSe ₂	3.28	15

5.3.3 Dependence of interlayer distance

In a comprehensive analysis of interlayer distance, binding energy (E_B) between the graphene and MoS₂ layers was calculated by $E_B = E_{(M/G)} - (E_M + E_G)$, where $E_{(M/G)}$, E_M , and E_G are the total energies for the graphene-MoS₂, monolayer MoS₂,

and monolayer graphene, respectively, and the results are shown in Fig.5.6. At an optimized interlayer distance of 3.38 Å, the calculated E_B reaches its lowest value of -22 meV, which corresponds with the previous work[136].

The dependence of bandgap on the interlayer distance in the graphene-MoS₂ is shown in the Fig. 5.7. We set the interlayer distance varies from 2.6 to 3.6 Å. As seen in the figure, at the optimum state of 3.38 Å of interlayer distance, the bandgap is 8.5 meV. The band gap is found to decrease when the interlayer distance increases gradually. Thus, widening interlayer distance between graphene and MoS₂ layers diminishes the orbital hybridization between the layers, leading to a pure graphene-like electronic structure that has no bandgap.

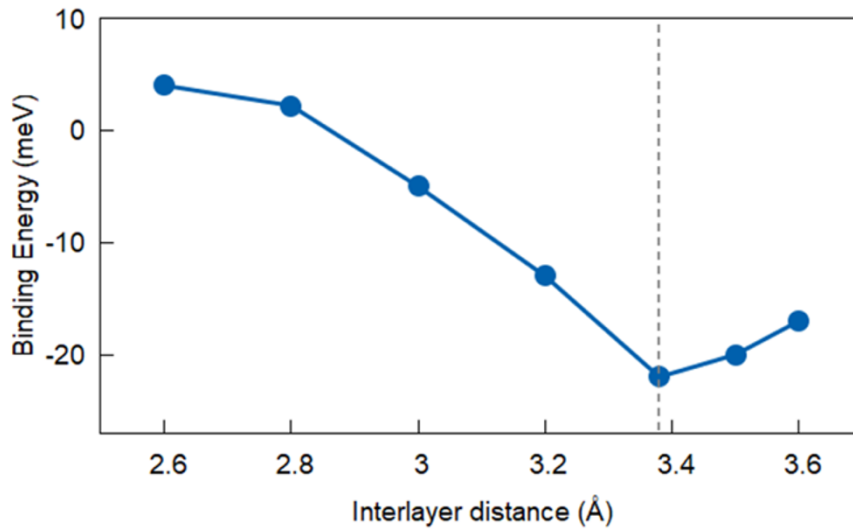


Figure 5.6: Binding energy as a function of interlayer distance

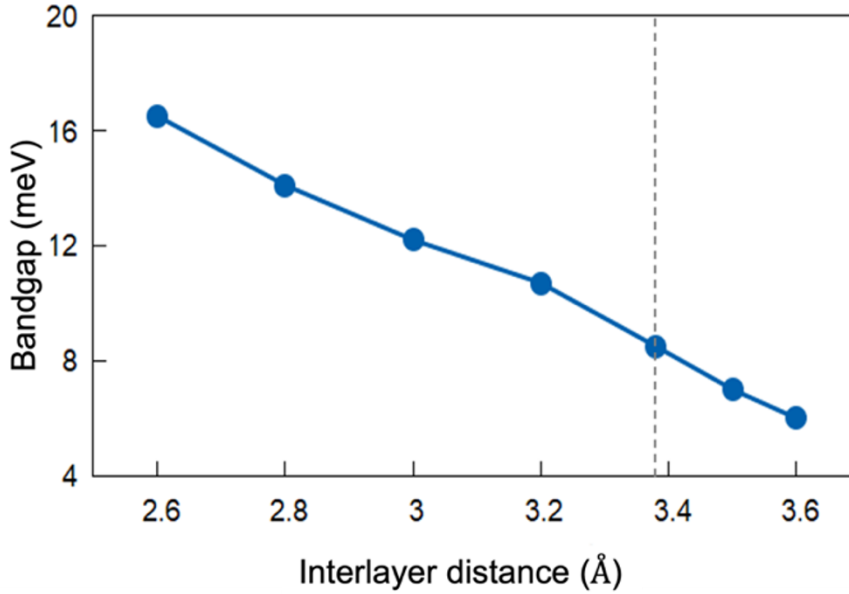


Figure 5.7: Bandgap in function of interlayer distance

5.4 Concluding Remarks

We utilized first-principles calculations to investigate the impact of stacking orientation, element substitution, and interlayer distance on the electronic structures of graphene-MoS₂ heterostructures. These findings suggest that the stacking orientation has minimal effect on the electronic properties of the heterostructure. However, we observed that element substitution significantly modifies the electronic properties of the system, leading to the opening of the bandgap and transformation into a metal characteristic.

Additionally, this research indicates that the bandgap opening in the graphene-MoS₂ heterostructure can be adjusted by modifying the interlayer distance. Overall, these results provide valuable insight into the electronic properties of graphene-MoS₂ heterostructures and offer potential method for tuning their properties through element substitution and interlayer distance modification.

Chapter 6

Graphene-MoS₂ heterostructure with external electric field

6.1 Introduction

Due to their fascinating electrical, thermal, and optical characteristics, two-dimensional (2D) van der Waals (vdW) materials like graphene and transition metal dichalcogenides (TMDs) have lately attracted growing interest in 2D material research area [110, 119, 137]. Graphene, especially, is the most well-known 2D material with a hexagonal structure that shows small intrinsic spin-orbit coupling (SOC), which is able to transport spins over tens of micrometers [138, 139]. Because of the same factor, however, the spin current control in graphene is not feasible, restricting its use in spintronics technology. In order to solve this limitation, some method to artificially induce the effect of SOC in graphene have been reported previously, such as chemical dopings [140, 68] and combining graphene and other material with large SOC as a heterostructure [141, 142]. Numerous previous studies have been done to model van der Waals graphene-TMD, e.g. graphene-MoS₂ [143], graphene-MoTe₂ [144], and graphene-WSe₂ [145].

On the other hand, TMDs possess larger intrinsic SOC [35], and can be hybridized into graphene by forming heterostructures. The proximity-induced SOC in graphene by TMD contribution has been the topic of a number studies conducted over the past several years, most notably in graphene-MoS₂, where the research reported Rashba SOC strength of 0.9 meV in the heterostructure [36]. Omar and van Wees recently reported that they were able to measure spin injection into graphene through WS₂

layer, as well as tuning interface resistance and spin injection efficiency by applying a voltage bias between layers [37]. Dankert and Dash successfully demonstrated electric gate control of spin current and spin lifetime, which also tune Schottky barrier of graphene-MoS₂ [34]. Another study observed bandgap of 17 meV in graphene acquired from constructing graphene-WS₂ [38].

Spin Hall effect (SHE), as one of the most remarkable properties to generate a transverse spin-current, so-called spin conversion, is currently intensively studied. The prior works demonstrate different ways to tune spin Hall conductivity (SHC), for example, by stacking-orientation controlling of bilayer structure [39], Fermi-energy tuning [40], and applying an external electric field [41]. The spin-to-charge conversion process caused by inverse SHE in MoS₂ and graphene induced inverse Rashba-Edelstein effect was recently observed experimentally [141]. Li *et al.* theoretically predicted that photonic SHE on graphene-MoS₂ explores the possibility of this heterostructure to be applied in highly-sensitive biosensor [146]. A recent study introduced a weak-value amplification measurement technique for precise detection of spin Hall shift in monolayer MoS₂, which makes it more convenient for spin-related applications [147]. Garcia *et al.* reported the enhancement of SHE in graphene-MoS₂, which originates from the valley-Zeeman type SOC preserved from TMD to graphene (i.e., the proximity-induced SOC in graphene due to a weak hybridization with TMD) [148].

6.2 Calculation Model

First-principles calculations using full-potential linearized augmented plane-wave approach with a single slab geometry were performed [63]. Exchange correlation of generalized gradient approximation was employed [93], and DFT-D2 approach was established to account for long-range dispersion correction [130]. Muffin-tin (MT) sphere radii of 2.6 Bohr for Mo, 1.9 Bohr for S, and 1.2 Bohr for C were used. The cutoff energy of plane-wave basis was set to 3.9 Bohr⁻¹, and a 45 × 45 *k*-point mesh was used for self-consistent field calculations. A homogenous external electric field up to ±0.6 V/Å was applied along the *z*-axis, i.e., perpendicular to the surface plane as shown in Fig. 6.1(a), such that positive (negative) electric field will induce accumulation (depletion) of electrons at the graphene side. As for a model, a graphene-MoS₂ heterostructure with an AB stacking with hexagonal lattice was used, as illustrated in Fig.6.1, where S atoms are located in the center of the hexagonal C sites, and Mo atoms are located on

the top of C atoms. An in-plane lattice constant of 3.1 Å [149], was employed while the structural periodicity in graphene and MoS₂ layers was assumed to be a 1:1 ratio, which consists of 1×1 cell in graphene and MoS₂. All atomic positions were fully optimized by atomic force calculations. And 491 × 491 \mathbf{k} -point mesh was used to calculate the SHC.

Spin Berry curvature in the first Brillouin zone was used to derive SHC based on linear response Kubo formula in the static limit. The SHC, the in-plane off-diagonal conductivity, can be obtained by an integration of spin Berry curvature as,

$$\sigma_{xy}^s = \sum_{\mathbf{k}}^{BZ} \Omega_{xy}^s(\mathbf{k}),$$

$$\Omega_{xy}^s(\mathbf{k}) = \sum_{m \neq n} \frac{\text{Im}[\langle m, \mathbf{k} | \hat{v}_x^s | n, \mathbf{k} \rangle \langle n, \mathbf{k} | \hat{v}_y | m, \mathbf{k} \rangle]}{[\epsilon_m(\mathbf{k}) - \epsilon_n(\mathbf{k})]^2}, \quad (6.1)$$

where Ω_{xy}^s represents spin Berry curvature, $\epsilon_m(\mathbf{k})$ and $\epsilon_n(\mathbf{k})$ indicate calculated eigenvalues of occupied state $|m, \mathbf{k}\rangle$ and unoccupied state $|n, \mathbf{k}\rangle$, respectively. \hat{v}_y and \hat{v}_x^s are charge and spin velocity operators and the latter is $\frac{1}{2}\{\sigma_z, \hat{v}_x\}$ [150], where σ_z is spin Pauli matrix with spin axis along the surface normal.

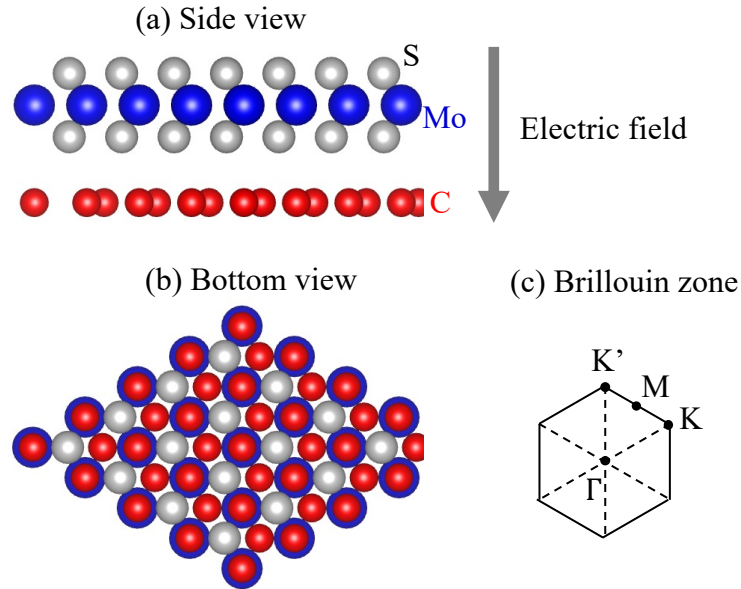


Figure 6.1: (a) and (b) Side and bottom views of graphene-MoS₂ heterostructure where blue, silver, and red colors represent Mo, S, and C atoms, respectively. An external electric field is applied along the surface normal where a positive electric field is defined by a grey arrow in (a). (c) A 2D Brillouin zone of graphene-MoS₂ heterostructure and symbols represent high symmetry \mathbf{k} -points used in the present work.

6.3 Electric polarization and electron density

We first present the electric polarization along the out-of-plane direction, calculated by

$$P_z = \int_{-\infty}^{\infty} z\rho(\mathbf{r}) d\mathbf{r} \quad (6.2)$$

in the single slab geometry, where $\rho(\mathbf{r})$ includes electron and nucleus charges. The results are shown in Fig.6.2(a). The electric polarization is found to linearly increase as the electric field increases.

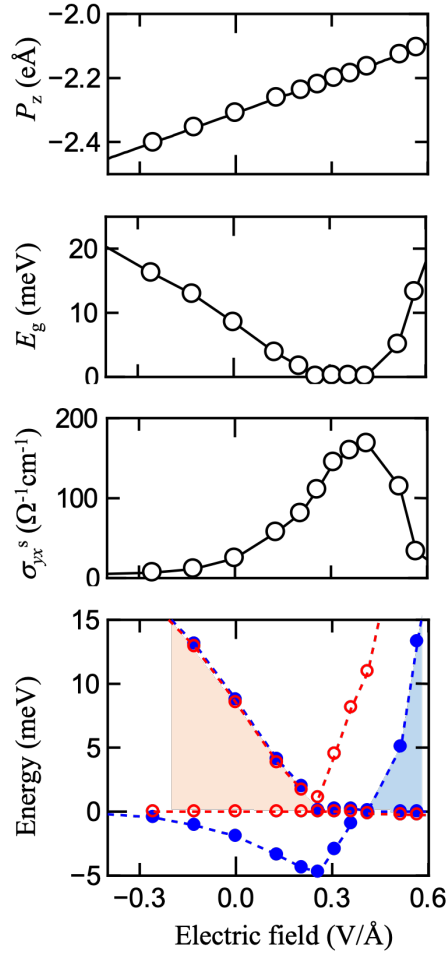


Figure 6.2: (a)-(d) Bandgap, electric polarization, spin Hall conductivity, and energy of eigen states as a function of electric field from -0.26 to 0.51 V/Å. In (d), red open circles and blue closed circles represent the spin-down and spin-up states around Fermi level at K, and white, blue, and orange vertical shades indicate electronic states of insulator, *n*-type metal, and *p*-type metal states, respectively.

In order to examine the microscopical mechanism in the electric polarization, the

difference in electron density distribution was defined by $\Delta n(\mathbf{r}) = n_{\text{MoS}_2/\text{graphene}}(\mathbf{r}) - n_{\text{graphene}}(\mathbf{r}) - n_{\text{MoS}_2}(\mathbf{r})$, where electron densities of graphene and MoS₂, $n_{\text{graphene}}(\mathbf{r})$ and $n_{\text{MoS}_2}(\mathbf{r})$, are obtained from the isolated free standing layers, respectively, with atomic positions fixed to those in graphene-MoS₂ heterostructure and subtracted from that of the whole heterostructure $n_{\text{MoS}_2/\text{graphene}}$. The results for zero electric field and ± 2.6 V/Å are shown in Fig.6.3, where yellow and blue colors represent positive and negative values with an absolute value of 10^{-5} electrons/Bohr³.

At zero electric field, in Fig.6.3(b), the electron density increases at the interface between graphene and MoS₂ layers (yellow portion), which illustrates a weak layer-layer interaction in the graphene-MoS₂. The electron density around the graphene layer slightly decreases (blue portion). Inside the MoS₂ layer, however, there is almost no change in the electron density distribution.

The distribution of the electron density in the graphene-MoS₂ has an asymmetric response to the applied electric field. At the positive electric field [Fig.6.3(c)], the electrons deplete on the top and accumulates on the bottom of MoS₂ layer. Meanwhile at the negative electric field [Fig.6.3(a)], the electrons accumulate on the top end of the MoS₂ layer compared to that in zero electric field, while at the bottom of the MoS₂ layer, i.e., at the interface, the electrons deplete. Interestingly, the electron density around the graphene layer does not alter much to that in zero electric field. Thus, the electron density on the graphene layer has almost no perturbation by the electric field so as to maintain charge neutrality. In another word, the electric-field-induced electron accumulation/depletion at both end of the MoS₂ layer acts as an electric double-layer capacitor [151], which gives a strong electric field to the neighboring graphene.

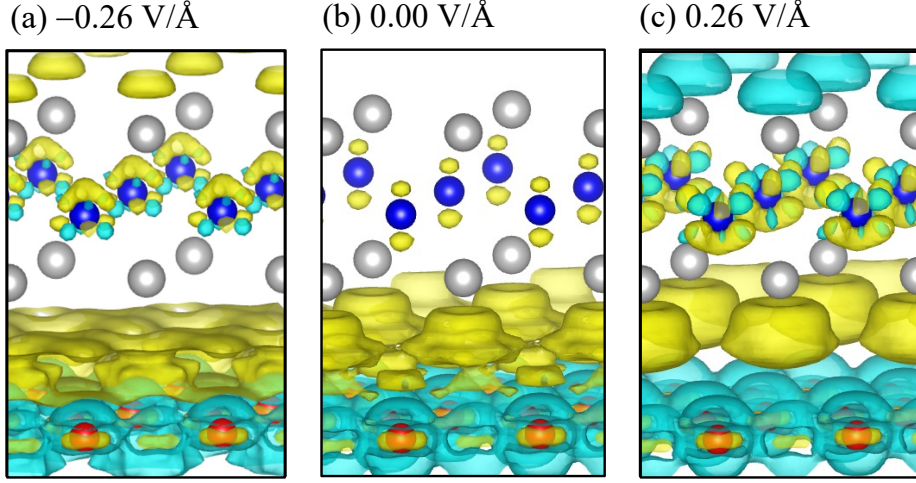


Figure 6.3: Electron density distribution of heterostructure for external electric fields of (a) -0.26 V/\AA , (b) 0.00 V/\AA , and (c) 0.26 V/\AA , which show contrast reaction for negative and positive electric fields. Yellow color represents an accumulation of electrons while the blue color shows an electron depletion with an absolute value of 10^{-5} electrons/Bohr³.

6.4 Electronic structure

Figure 6.4(b) shows the band structure along the high symmetry in-plane \mathbf{k} -directions [see in Fig. 6.1(c)] for the graphene-MoS₂ in zero electric field. Two characteristic features in band dispersion are visible, which mainly arise from the MoS₂ and graphene layers, respectively; the former and latter are shown with and without green shades in the left figure of Fig. 6.4(b). The bands of MoS₂ have less dispersion and have a large energy separation between the valence and conduction states by about 1.71 eV showed by a dashed arrow, which behaves almost as a freestanding MoS₂ monolayer (with the bandgap of 1.82 eV [152]) or bilayer (1.7 eV) [153]. In contrast, the dispersive bands of graphene have Dirac points at K and K'. Both MoS₂ and graphene bands weakly hybridize each other, e.g., from K to Γ at around 2.2 eV and from K to M (K' to M) at around -1.5 eV, at which the crossing bands are lifted with small energy gaps of about 0.1 eV.

A valley structure with direct bandgaps of 8.53 meV at both K and K' is confirmed as shown in the enlarged figure at the right of Fig. 6.4(b), which are in contrast to the zero-bandgap of freestanding graphene [1]. The results indicate that the bandgap opening due to the SOC can be introduced in the graphene-MoS₂ through the weak

hybridization. In the valence edges at Dirac points, the spin degeneracy along to the out-of-plane direction is lifted into the opposite spin states, spin-up (blue line) and spin-down (red line), being consisted of the C p_z orbitals, with a splitting of about 2 meV, which is close to the previous theoretical study of other TMD material with similar characteristic of graphene-WSe₂ (2.54 and 2.51 meV) [122, 154]. For the conduction edges, in contrast, the opposite spin states are nearly degenerated, importantly consisting of the C p_z orbital with a mixture of C p_x and p_y orbitals.

Figure 6.4(a-c) shows how electric field affects band structure of the graphene-MoS₂. We find that the energy positions of the MoS₂ bands (green shades) highly depend on the electric field. When the negative electric field is applied, the MoS₂ bands shift down in energy with respect to the Dirac points so that the MoS₂ conduction state is close to the Dirac point, while for the positive electric field, the MoS₂ bands go up where the MoS₂ valence state is approaching the Dirac points. As seen in the right figures of Fig. 6.4(a-c), the negative electric field of -0.26 V/\AA gives a much wider bandgap of 16.2 meV in the Dirac points, almost double the bandgap of zero-field structure. Meanwhile, the positive electric field of 0.26 V/\AA transforms the state to a metallic with hole pockets at K and K', where the valence top at K and K' exceeds the Fermi level.

The electric field dependence of the bandgap at K is illustrated in Fig.6.2(b). Below 0.2 V/\AA , the bandgap changes linearly as the electric field increases so that the bandgap is controllable by using an electric field with a slope of $50 \text{ meV}/(\text{V/\AA})$. In a range of the electric field at between 0.2 to 0.51 V/\AA , however, it is metallic, and when the electric field further increases above 0.51 V/\AA , the bandgap is opened again.

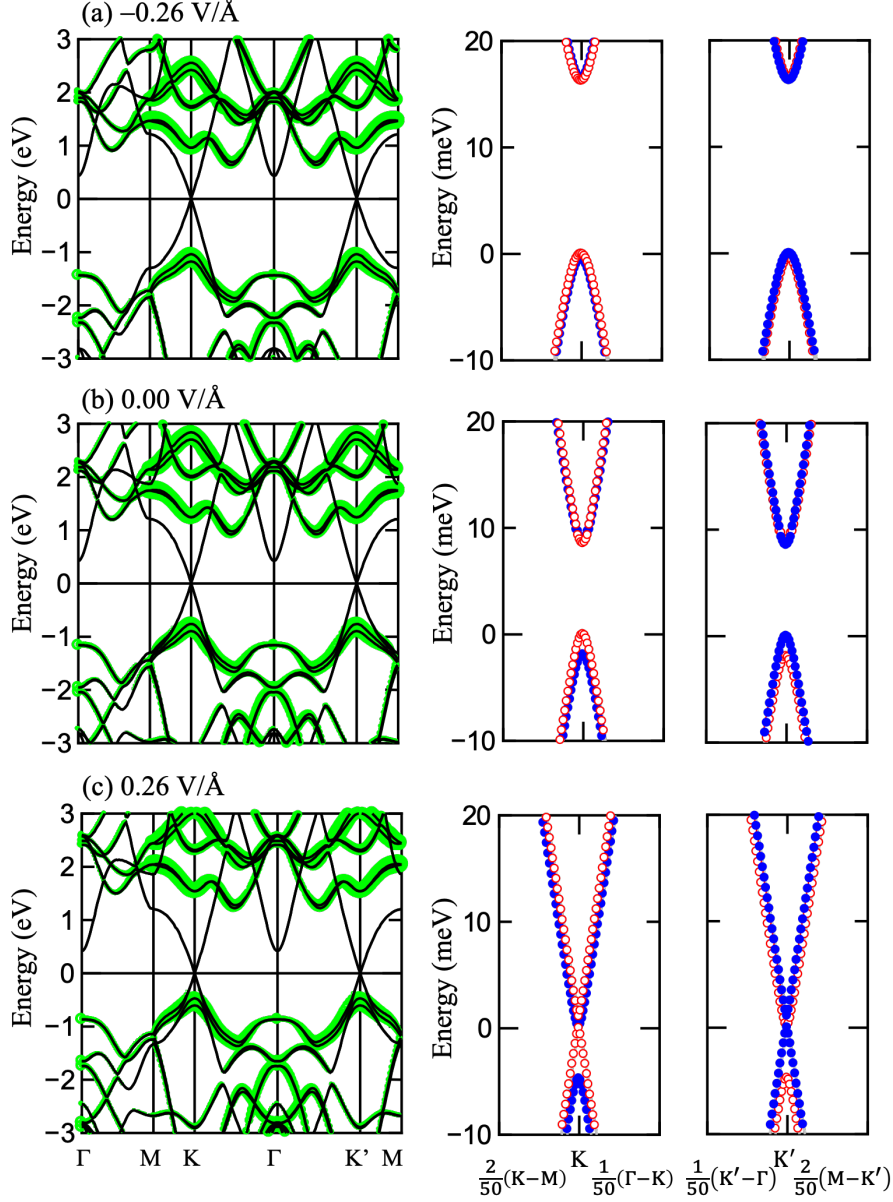


Figure 6.4: The left and right figures represent calculated band structure and Dirac points at K and K', respectively, for electric fields of (a) -0.26 V/\AA , (b) 0.00 V/\AA , and (c) 0.26 V/\AA . Green shades on the left figures show the weight of wavefunction of MoS₂. Red and blue circles in the right figures represent the spin-down and spin-up states projected along to the surface normal.

6.5 Spin Hall Conductivity

The calculated SHC, $-\sigma_{xy}^s$, of the graphene-MoS₂ as a function of the electric field is shown in Fig. 6.2(c). At zero electric field, the $-\sigma_{xy}^s$ of $25 \text{ } \Omega^{-1}\text{cm}^{-1}$ was obtained. Although the absolute value is small compared to the typical value of bulk Pt, $2200 \text{ } \Omega^{-1}\text{cm}^{-1}$ [155], by two orders of magnitude, it is larger than that of bilayer graphene

of close-to-zero [153], indicating that the combination of graphene and MoS₂ causes the SHC. The negative electric field does not give a larger change in the SHC, while for the positive electric field, the value is significantly enhanced compared to that in zero electric field and has a peak of about 170 Ω⁻¹cm⁻¹ at around 0.4 V/Å. When the electric field is over 0.5 V/Å, the SHC rapidly decreases.

The \mathbf{k} -dependence of the SHC, $-\sigma_{xy}^s(\mathbf{k})$, were calculated, and the results at zero electric field and ± 0.26 V/Å are shown in Fig. 6.5. In zero electric field [Fig. 6.5(b)], the $-\sigma_{xy}^s(\mathbf{k})$ shows small value in the whole \mathbf{k} space except at K and K'. At K and K', however, there are large positive and negative peaks so that the magnitude of SHC is enhanced. Thus, the large SHC comes from the Dirac points at K and K'. The same phenomenon is also occurred at negative electric field [Fig.6.5(a)] and positive electric field [Fig.6.5(c)].

To discuss more details, the band structure and the \mathbf{k} -dependence of $-\sigma_{xy}^s(\mathbf{k})$ at around K along M-K-Γ in a variation of electric field from zero to 0.51 V/Å are shown in the top- and the second-rows in Fig. 6.6, where blue and red circles in the top figures represent the spin-up and spin-down states, respectively. We further examined the pair contribution between bands m and n to the spin Berry curvature, defined as,

$$\Omega_{xy,(m,n)}^s = \frac{\text{Im}[\langle m, \mathbf{k} | \hat{v}_x^s | n, \mathbf{k} \rangle \langle n, \mathbf{k} | \hat{v}_y | m, \mathbf{k} \rangle]}{[\epsilon_n(\mathbf{k}) - \epsilon_m(\mathbf{k})]^2} \quad (6.3)$$

The matrix elements of velocity, e.g., $\Pi_x = \langle m, \mathbf{k} | \hat{v}_x | n, \mathbf{k} \rangle$, by introducing $\Pi_{\pm} = \Pi_x \pm i\Pi_y$, correspond to electric dipole transitions with selection rules of $\Delta l = \pm 1$ and $\Delta m = \pm 1$ for angular and magnetic quantum numbers. The results at around K are shown in the third-row in Fig. 6.6. In the present system, an orbital mixture of p_x and p_y by the SOC as presented in Sec.3.1, as well as small the energy splitting in the Dirac bands, gives SHC. At zero electric field [Fig. 6.6(a)], as mentioned in Fig. 6.2, the two bands at the valence top at K, bands 25 and 26, are lifted by the SOC with an energy splitting of 2 meV and the two bands at the conduction bottom, bands 27 and 28, are lifted.

However, when the electric field increases to 0.26 V/Å, the conduction edge of spin-down states (red plot) touches to the band $m = 26$ at the Fermi energy, i.e., the system transforming to the metallic, and eventually the sign of $\Omega_{yx,26}^s(\mathbf{k})$ changes to the positive due to the band inversion [122]. Thus, the bands of $m = 25$ and 26 contribute

with the same sign and the SHC is enhanced.

When the electric field further increases (0.36 V/\AA) [Fig. 6.6(b)], the band $m = 25$ shifts up and touches the conduction edge of spin-up states (blue plot), giving significant contribution of $\Omega_{yx,25}^s(\mathbf{k})$, while the conduction edge of spin-down states (red) moves away from the Fermi energy giving small $\Omega_{yx,26}^s(\mathbf{k})$. However, the band gap is opened again by applying electric field of 0.51 V/\AA . Consequently, $\Omega_{yx,m}^s(\mathbf{k})$ ($m = 25$ and 26) becomes small due to the large value of the denominator in Eq. (6.3), resulting in a small SHC.

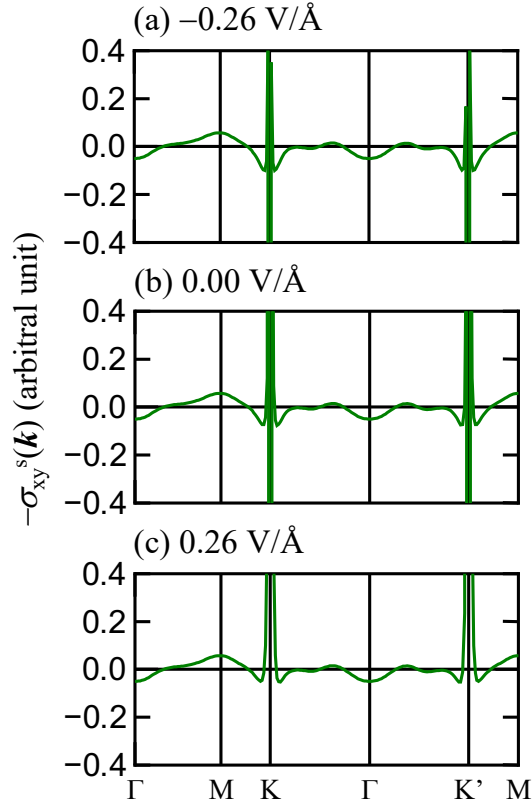


Figure 6.5: \mathbf{k} -dependence of spin Hall conductivity for external electric fields of (a) -0.26 V/\AA , (b) 0.00 V/\AA , and (c) 0.26 V/\AA . The positive and negative peaks are found at K and K', associated with the location of Dirac points.

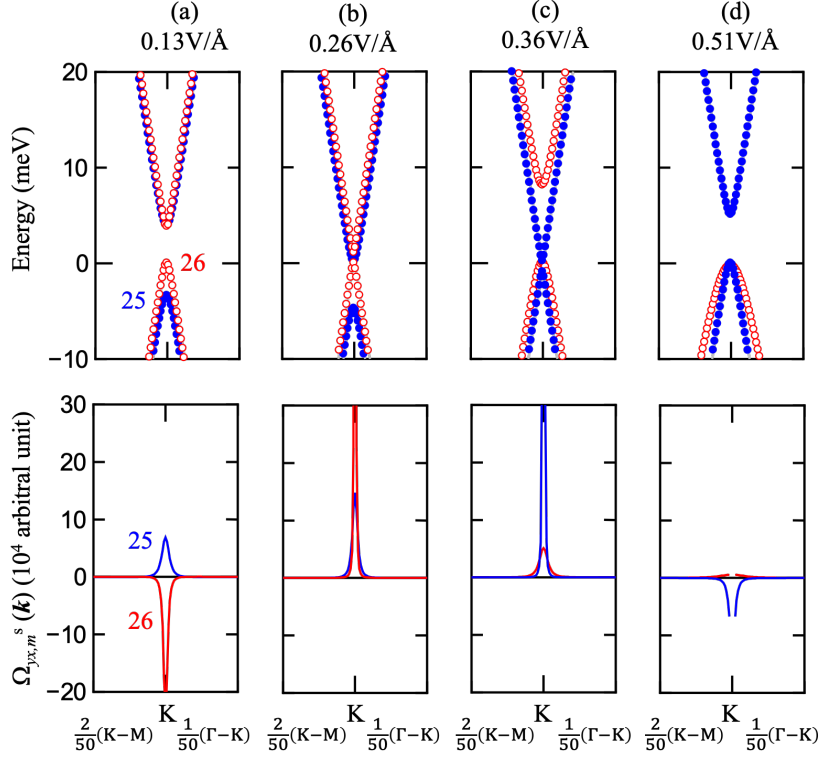


Figure 6.6: Band structure around K (top) and corresponding spin Berry curvature $\Omega_{yx,m}^s$ (bottom) under electric fields of (a) 0.13, (b) 0.26, (c) 0.36, (d) 0.51 V/Å, where numbers (25 and 26) indicate band indexes (m). In top panels, blue and red circles represent the spin-up and -down states, and in bottom panels, blue and red lines represent spin Berry curvature in Eq. (2) of concerned bands. Zero energy sets to an energy of the valence edge.

6.6 Concluding Remarks

By employing first-principles calculations, these findings indicate that the SHC of the heterostructure can be adjusted by varying the magnitude of the applied electric field. We have observed that an increase in the electric field results in a boost in polarization along the out-of-plane direction, primarily caused by the MoS₂ layer. Furthermore, we have discovered that the bandgap opening can be controlled with a slope of -50 meV/V/Å.

In addition, we have examined the impact of the electric field on the spin-splitting of the band structure by applying an external electric field. The results show that the electric field causes a significant change in the SHC, particularly with positive electric fields, while negative electric fields have minimal impact on SHC control. These findings

provide valuable insight into the manipulation of SHC in van der Waals heterostructures and offer a new approach for the design and optimization of electronic devices. The ability to control the SHC through electric field modulation could potentially lead to the development of more efficient and high-performance electronic devices in the future.

Chapter 7

Conclusions and prospects

In this thesis, we present first-principles study of electric field effects on graphene-based structures for battery and spintronic materials application. The introduction, background, and motivation are stated in chapter one.

Chapter two present the theory and method in calculations. We briefly explain the concept of density functional theory (DFT) and full-potential linearized augmented plan wave (FLAPW) method which we apply in the calculations. We also defining the van der Waals approximation for the calculation.

In chapter three of this research, various materials such as graphene, germanene, and the defected structures were constructed and analyzed to comprehend their electronic and structural properties. The calculation of monovacancy in monolayer graphene and monolayer germanene revealed that monovacancy germanene has lower formation energy than monovacancy graphene due to low buckling germanene by 5.5 eV. The investigation also encompassed germanene, with a particular focus on examining the stability of germanene multivacancy. It was further conducted on multivacancy in germanene where the most stable multivacancy structures is consisted of even-numbered vacancies. The appropriate structures identified through this study will be used for further calculations.

Chapter four of this study presents an investigation of defected-bilayer graphene. The main objective was to examine the intercalation of lithium in defected-bilayer graphene as a means of developing more effective energy storage systems. This research revealed that the application of an external electric field can significantly enhance lithium stability in defected-bilayer graphene, proven by lower adsorption energy, leading to a lower intercalation energy required for the intercalation process. This study

proposes an approach to further enhance the capacity for lithium by utilizing an electric field that effectively increase the capacity to accommodate 12 lithium atoms. This result shows 140% increasement of capacity of lithium compared to pristine bilayer graphene.

In the chapter five, we constructed a graphene-MoS₂ heterostructure. We identify the effect of stacking orientation, element substitution, and interlayer distance on the electronic structure of the heterostructure. We find that the stacking orientation has minimal effect on the electronic properties of the heterostructure. However, we observed that the results indicate that the electronic structures are not significantly influenced by the stacking orientation, in contrast to how element substitution and interlayer distance successfully modify them. Bandgap opening is importantly emerged by forming the heterostructure via a symmetry breaking of carbon staking-sites on MoS₂. The findings are crucial for further research aimed at manipulating the electronic properties of graphene-MoS₂ heterostructure.

In chapter six, the influence of an external electric field on bandgap opening and spin Hall conductivity in graphene-MoS₂ heterostructure was investigated. As a result, an increase in the electric field induced an out-of-plane polarization, primarily driven by the presence of MoS₂, resulting in insulator to metallic transformation of the heterostructure which led to increase in spin Hall conductivity up to $170 \Omega^{-1} \text{ cm}^{-1}$. These findings demonstrate the potential of spin generation in graphene-MoS₂ heterostructure through spin Hall conductivity, which can be tuned by an electric field. These results open up possibilities for the application of graphene-MoS₂ heterostructure in spintronics applications.

Finally, this dissertation shows an excellent way to tune electronic structure and spin Hall conductivity in graphene-MoS₂ heterostructure, as well as the intercalation of lithium in bilayer graphene. These findings provide valuable insight into the manipulation of SHC in van der Waals heterostructures and offer a new approach for the design and optimization of electronic devices. The ability to control the SHC through electric field modulation could potentially lead to the development of more efficient and high-performance spintronic devices in the future. We also propose a method to increase the lithium capacity in defected-bilayer graphene by applying electric field. With more research and development, it's likely that bilayer graphene will become more important in the improvement of Li-ion batteries and the move towards energy storage systems that are better for the environment and more effective.

Bibliography

- [1] K. S. Novoselov, A. K. Geim, S. V. Morozov, D. Jiang, Y. Zhang, S. V. Dubonos, I. V. Grigorieva, and A. A. Firsov, “Electric field effect in atomically thin carbon films,” *Science*, vol. 306, no. 5696, pp. 666–669, 2004.
- [2] K. S. Novoselov, A. K. Geim, S. V. Morozov, D. Jiang, M. I. Katsnelson, I. V. Grigorieva, S. V. Dubonos, and A. A. Firsov, “Two-dimensional gas of massless dirac fermions in graphene,” *Nature*, vol. 438, pp. 197–200, 2005.
- [3] A. K. Geim and K. S. Novoselov, “The rise of graphene progress,” *Nature Materials*, vol. 6, pp. 183–191, 2007.
- [4] L. Liao, H. Peng, and Z. Liu, “Chemistry makes graphene beyond graphene,” *Journal of the American Chemical Society*, vol. 136, pp. 12 194–12 200, 9 2014.
- [5] G. W. Flynn, “Atomic scale imaging of the electronic structure and chemistry of graphene and its precursors on metal surfaces,” *Columbia Univ., New York, NY*, vol. 1, no. 2, 2 2015.
- [6] C. Lee, X. Wei, J. W. Kysar, and J. Hone, “Measurement of the elastic properties and intrinsic strength of monolayer graphene,” *Science*, vol. 321, no. 5887, pp. 385–388, 2008.
- [7] R. Geetha Bai, K. Muthoosamy, F. N. Shipton, and S. Manickam, “Acoustic cavitation induced generation of stabilizer-free, extremely stable reduced graphene oxide nanodispersion for efficient delivery of paclitaxel in cancer cells,” *Ultrasonics Sonochemistry*, vol. 36, p. 129–138, 2017.
- [8] Z. Bai, C. Zhou, H. Xu, G. Wang, H. Pang, and H. Ma, “Polyoxometalates-doped au nanoparticles and reduced graphene oxide: A new material for the detection of uric acid in urine,” *Sensors and Actuators B: Chemical*, vol. 243, pp. 361–371, May 2017.

-
- [9] B. Han, J. Song, T. Hu, H. Ye, and L. Xu, “High thermal conductivity in polydimethylsiloxane composite with vertically oriented graphene nanosheets by liquid-phase exfoliation,” *Chemical Physics Letters*, vol. 743, p. 137156, Mar. 2020.
- [10] M. Zeng, Y. Xiao, J. Liu, K. Yang, and L. Fu, “Exploring two-dimensional materials toward the next-generation circuits: From monomer design to assembly control,” *Chemical Reviews*, vol. 118, no. 13, pp. 6236–6296, Jan. 2018.
- [11] E. Golias, E. Xenogiannopoulou, D. Tsoutsou, P. Tsipas, S. A. Giamini, and A. Dimoulas, “Surface electronic bands of submonolayer ge on ag(111),” *Phys. Rev. B*, vol. 88, p. 075403, Aug 2013.
- [12] W.-S. Kim, Y. Hwa, J.-H. Shin, M. Yang, H.-J. Sohn, and S.-H. Hong, “Scalable synthesis of silicon nanosheets from sand as an anode for li-ion batteries,” *Nanoscale*, vol. 6, no. 8, p. 4297, 2014.
- [13] A. O’Hare, F. V. Kusmartsev, and K. I. Kugel, “A stable form of two-dimensional crystals: Could graphene, silicene, germanene be minigap semiconductors?” *Nano Letters*, vol. 12, no. 2, pp. 1045–1052, Jan. 2012.
- [14] M. Houssa, G. Pourtois, V. V. Afanasev, and A. Stesmans, “Electronic properties of two-dimensional hexagonal germanium,” *Applied Physics Letters*, vol. 96, no. 8, p. 082111, Feb. 2010.
- [15] X.-S. Ye, Z.-G. Shao, H. Zhao, L. Yang, and C.-L. Wang, “Intrinsic carrier mobility of germanene is larger than graphenes: first-principle calculations,” *RSC Adv.*, vol. 4, no. 41, pp. 21 216–21 220, 2014.
- [16] B. Bishnoi and B. Ghosh, “Spin transport in silicene and germanene,” *RSC Advances*, vol. 3, no. 48, p. 26153, 2013.
- [17] R. wu Zhang, W. xiao Ji, C. wen Zhang, S. shi Li, P. Li, P. ji Wang, F. Li, and M. juan Ren, “Controllable electronic and magnetic properties in a two-dimensional germanene heterostructure,” *Physical Chemistry Chemical Physics*, vol. 18, no. 17, pp. 12 169–12 174, 2016.

-
- [18] H. Li, J. Wu, Z. Yin, and H. Zhang, "Preparation and applications of mechanically exfoliated single-layer and multilayer MoS nanosheets," *Accounts of Chemical Research*, vol. 47, no. 4, pp. 1067–1075, Apr. 2014.
- [19] X.-R. Wang, Y. Shi, and R. Zhang, "Field-effect transistors based on two-dimensional materials for logic applications," *Chinese Physics B*, vol. 22, no. 9, p. 098505, Sep. 2013.
- [20] Z. Yin, H. Li, H. Li, L. Jiang, Y. Shi, Y. Sun, G. Lu, Q. Zhang, X. Chen, and H. Zhang, "Single-layer MoS phototransistors," *ACS Nano*, vol. 6, no. 1, pp. 74–80, Dec. 2011.
- [21] E. Lee, Y. S. Yoon, and D.-J. Kim, "Two-dimensional transition metal dichalcogenides and metal oxide hybrids for gas sensing," *ACS Sensors*, vol. 3, no. 10, pp. 2045–2060, Oct. 2018.
- [22] Q. Peng and S. De, "Outstanding mechanical properties of monolayer MoS₂ and its application in elastic energy storage," *Physical Chemistry Chemical Physics*, vol. 15, no. 44, p. 19427, 2013.
- [23] S. Pescetelli, A. Agresti, G. Viskadourous, S. Razza, K. Rogdakis, I. Kalogerakis, E. Spiliarotis, E. Leonardi, P. Mariani, L. Sorbello, M. Pierro, C. Cornaro, S. Bellani, L. Najafi, B. Martín-García, A. E. D. R. Castillo, R. Oropesa-Nuñez, M. Prato, S. Maranghi, M. L. Parisi, A. Sinicropi, R. Basosi, F. Bonaccorso, E. Kymakis, and A. D. Carlo, "Integration of two-dimensional materials-based perovskite solar panels into a stand-alone solar farm," *Nature Energy*, vol. 7, no. 7, pp. 597–607, Jun. 2022.
- [24] V. H. Guarocho-Moreira, J. L. Sambricio, K. Omari, C. R. Anderson, D. A. Bandurin, J. C. Toscano-Figueroa, N. Natera-Cordero, K. Watanabe, T. Taniguchi, I. V. Grigorieva, and I. J. Vera-Marun, "Tunable spin injection in high-quality graphene with one-dimensional contacts," *Nano Letters*, vol. 22, no. 3, pp. 935–941, Jan. 2022.
- [25] Z. Liu, Z. Lou, Z. Li, G. Wang, Z. Wang, Y. Liu, B. Huang, S. Xia, X. Qin, X. Zhang, and Y. Dai, "GeH: a novel material as a visible-light driven photocatalyst for hydrogen evolution," *Chem. Commun.*, vol. 50, no. 75, pp. 11 046–11 048, 2014.

-
- [26] S. Jiang, K. Krymowski, T. Asel, M. Q. Arguilla, N. D. Cultrara, E. Yanchenko, X. Yang, L. J. Brillson, W. Windl, and J. E. Goldberger, "Tailoring the electronic structure of covalently functionalized germanane via the interplay of ligand strain and electronegativity," *Chemistry of Materials*, vol. 28, no. 21, pp. 8071–8077, Oct. 2016.
- [27] M. R. Esmaeili-Rad and S. Salahuddin, "High performance molybdenum disulfide amorphous silicon heterojunction photodetector," *Scientific Reports*, vol. 3, no. 1, Aug. 2013.
- [28] H. Wu, Y. Wu, X. Chen, Y. Ma, M. Xu, W. Wei, J. Pan, and X. Xiong, "Rational design and preparation of few-layered MoS₂/nanobelt heterostructures with superior lithium storage performance," *RSC Advances*, vol. 6, no. 28, pp. 23 161–23 168, 2016.
- [29] J. Qiao, F. Feng, G. Cao, S. Wei, S. Song, T. Wang, X. Yuan, and M. G. Somekh, "Ultrasensitive near-infrared MoTe photodetectors with monolithically integrated fresnel zone plate metalens," *Advanced Optical Materials*, vol. 10, no. 15, p. 2200375, May 2022.
- [30] K. Ji, J. Han, A. Hirata, T. Fujita, Y. Shen, S. Ning, P. Liu, H. Kashani, Y. Tian, Y. Ito, J. ichi Fujita, and Y. Oyama, "Lithium intercalation into bilayer graphene," *Nature Communications*, vol. 10, no. 1, Jan. 2019.
- [31] D. T. Larson, S. Carr, G. A. Tritsarlis, and E. Kaxiras, "Effects of lithium intercalation in twisted bilayer graphene," *Phys. Rev. B*, vol. 101, p. 075407, Feb 2020.
- [32] J. Lin, Z. Peng, C. Xiang, G. Ruan, Z. Yan, D. Natelson, and J. M. Tour, "Graphene nanoribbon and nanostructured SnO composite anodes for lithium ion batteries," *ACS Nano*, vol. 7, no. 7, pp. 6001–6006, Jun. 2013.
- [33] F. Zhang, Z. Li, and F. Zhao, "Editorial: Advanced micro/nano materials for electrochemical energy conversion and application," *Frontiers in Energy Research*, vol. 10, Jan. 2023. [Online]. Available: <https://doi.org/10.3389/fenrg.2022.1047160>

-
- [34] A. Dankert and S. P. Dash, “Electrical gate control of spin current in van der waals heterostructures at room temperature,” *Nature Communications*, vol. 8, 7 2017.
- [35] K. F. Mak, C. Lee, J. Hone, J. Shan, and T. F. Heinz, “Atomically thin mos2: A new direct-gap semiconductor,” *Physical Review Letters*, vol. 105, 9 2010.
- [36] B. Yang, M. Lohmann, D. Barroso, I. Liao, Z. Lin, Y. Liu, L. Bartels, K. Watanabe, T. Taniguchi, and J. Shi, “Strong electron-hole symmetric rashba spin-orbit coupling in graphene/monolayer transition metal dichalcogenide heterostructures,” *Physical Review B*, vol. 96, 7 2017.
- [37] S. Omar and B. J. V. Wees, “Graphene- ws2 heterostructures for tunable spin injection and spin transport,” *Physical Review B*, vol. 95, 2 2017.
- [38] A. Avsar, J. Y. Tan, T. Taychatanapat, J. Balakrishnan, G. K. Koon, Y. Yeo, J. Lahiri, A. Carvalho, A. S. Rodin, E. C. O’Farrell, G. Eda, A. H. C. Neto, and B. Özyilmaz, “Spin-orbit proximity effect in graphene,” *Nature Communications*, vol. 5, 2014.
- [39] S. Li, Y. Liu, X. Zhao, Q. Shen, W. Zhao, Q. Tan, N. Zhang, P. Li, L. Jiao, and X. Qu, “Sandwich-like heterostructures of mos2/graphene with enlarged interlayer spacing and enhanced hydrophilicity as high-performance cathodes for aqueous zinc-ion batteries,” *Advanced Materials*, vol. 33, no. 12, p. 2007480, 2021.
- [40] J. Zhou, J. Qiao, A. Bournel, and W. Zhao, “Intrinsic spin hall conductivity of the semimetals mote2 and wte2,” *Physical Review B*, vol. 99, 2 2019.
- [41] P. T. Huong, D. Muoi, H. V. Phuc, C. V. Nguyen, L. T. Hoa, B. D. Hoi, and N. N. Hieu, “Low-energy bands, optical properties, and spin/valley-hall conductivity of silicene and germanene,” *Journal of Materials Science*, vol. 55, pp. 14 848–14 857, 10 2020.
- [42] S. Haffad, L. Benchallal, L. Lamiri, F. Boubenider, H. Zitoune, B. Kahouadji, and M. Samah, “Effect of vacancies on electronic and magnetic properties of hydrogen passivated graphene nanoribbons,” *Acta Physica Polonica A*, 2018.
- [43] A. K. Geim and I. V. Grigorieva, “Van der waals heterostructures,” *Nature*, vol. 499, no. 7459, pp. 419–425, Jul. 2013.

-
- [44] M.-Y. Li, C.-H. Chen, Y. Shi, and L.-J. Li, “Heterostructures based on two-dimensional layered materials and their potential applications,” *Materials Today*, vol. 19, no. 6, pp. 322–335, Jul. 2016.
- [45] W. J. Yu, Z. Li, H. Zhou, Y. Chen, Y. Wang, Y. Huang, and X. Duan, “Vertically stacked multi-heterostructures of layered materials for logic transistors and complementary inverters,” *Nature Materials*, vol. 12, no. 3, pp. 246–252, Dec. 2012.
- [46] F. Zhang, T. Li, L. Pan, A. Asthagiri, and J. F. Weaver, “CO oxidation on single and multilayer pd oxides on pd(111): mechanistic insights from RAIRS,” *Catal. Sci. Technol.*, vol. 4, no. 11, pp. 3826–3834, 2014.
- [47] W. J. Yu, Y. Liu, H. Zhou, A. Yin, Z. Li, Y. Huang, and X. Duan, “Highly efficient gate-tunable photocurrent generation in vertical heterostructures of layered materials,” *Nature Nanotechnology*, vol. 8, no. 12, pp. 952–958, Oct. 2013.
- [48] M. Shanmugam, R. Jacobs-Gedrim, E. S. Song, and B. Yu, “Two-dimensional layered semiconductor/graphene heterostructures for solar photovoltaic applications,” *Nanoscale*, vol. 6, no. 21, pp. 12 682–12 689, 2014.
- [49] Y. Gong, S. Lei, G. Ye, B. Li, Y. He, K. Keyshar, X. Zhang, Q. Wang, J. Lou, Z. Liu, R. Vajtai, W. Zhou, and P. M. Ajayan, “Two-step growth of two-dimensional WSe heterostructures,” *Nano Letters*, vol. 15, no. 9, pp. 6135–6141, Aug. 2015.
- [50] M. M. Furchi, A. Pospischil, F. Libisch, J. Burgdörfer, and T. Mueller, “Photovoltaic effect in an electrically tunable van der waals heterojunction,” *Nano Letters*, vol. 14, no. 8, pp. 4785–4791, Jul. 2014.
- [51] K. Zhang, X. Fang, Y. Wang, Y. Wan, Q. Song, W. Zhai, Y. Li, G. Ran, Y. Ye, and L. Dai, “Ultrasensitive near-infrared photodetectors based on a graphene-graphene vertical van der waals heterostructure,” *ACS Applied Materials and Interfaces*, vol. 9, no. 6, pp. 5392–5398, Feb. 2017.
- [52] S. Wang, J.-P. Chou, C. Ren, H. Tian, J. Yu, C. Sun, Y. Xu, and M. Sun, “Tunable schottky barrier in graphene/graphene-like germanium carbide van der waals heterostructure,” *Scientific Reports*, vol. 9, no. 1, Mar. 2019. [Online]. Available: <https://doi.org/10.1038/s41598-019-40877-z>

-
- [53] X. Li, Y. Dai, Y. Ma, S. Han, and B. Huang, “Graphene/g-c3n4 bilayer: considerable band gap opening and effective band structure engineering,” *Physical Chemistry Chemical Physics*, vol. 16, no. 9, p. 4230, 2014. [Online]. Available: <https://doi.org/10.1039/c3cp54592j>
- [54] K. Zollner, A. W. Cummings, S. Roche, and J. Fabian, “Graphene on two-dimensional hexagonal bn, aln, and gan: Electronic, spin-orbit, and spin relaxation properties,” *Phys. Rev. B*, vol. 103, p. 075129, Feb 2021.
- [55] E. Schrödinger, “Quantisierung als eigenwertproblem,” *Annalen der Physik*, vol. 384, no. 6, pp. 489–527, 1926. [Online]. Available: <https://doi.org/10.1002/andp.19263840602>
- [56] M. Born and R. Oppenheimer, “Zur quantentheorie der molekeln,” *Annalen der Physik*, vol. 389, no. 20, pp. 457–484, 1927. [Online]. Available: <https://doi.org/10.1002/andp.19273892002>
- [57] P. Hohenberg and W. Kohn, “Inhomogeneous electron gas,” *Phys. Rev.*, vol. 136, pp. B864–B871, Nov 1964.
- [58] J. C. Slater, “Wave functions in a periodic potential,” *Phys. Rev.*, vol. 51, pp. 846–851, May 1937.
- [59] O. K. Andersen, “Linear methods in band theory,” *Phys. Rev. B*, vol. 12, pp. 3060–3083, Oct 1975.
- [60] D. D. Koelling and G. O. Arbman, “Use of energy derivative of the radial solution in an augmented plane wave method: application to copper,” *Journal of Physics F: Metal Physics*, vol. 5, no. 11, pp. 2041–2054, Nov. 1975.
- [61] D. R. Hamann, “Semiconductor charge densities with hard-core and soft-core pseudopotentials,” *Phys. Rev. Lett.*, vol. 42, pp. 662–665, Mar 1979.
- [62] E. Wimmer, H. Krakauer, M. Weinert, and A. J. Freeman, “Full-potential self-consistent linearized-augmented-plane-wave method for calculating the electronic structure of molecules and surfaces: o₂ molecule,” *Phys. Rev. B*, vol. 24, pp. 864–875, Jul 1981.
- [63] K. Nakamura, T. Ito, A. J. Freeman, L. Zhong, and J. F. de Castro, “Enhancement of magnetocrystalline anisotropy in ferromagnetic fe films by intra-atomic

-
- noncollinear magnetism,” *Physical Review B - Condensed Matter and Materials Physics*, vol. 67, pp. 1–6, 2003.
- [64] S. Grimme, “Accurate description of van der waals complexes by density functional theory including empirical corrections,” *Journal of Computational Chemistry*, vol. 25, no. 12, pp. 1463–1473, 2004.
- [65] —, “Semiempirical GGA-type density functional constructed with a long-range dispersion correction,” *Journal of Computational Chemistry*, vol. 27, no. 15, pp. 1787–1799, 2006.
- [66] S. Grimme, J. Antony, T. Schwabe, and C. Mück-Lichtenfeld, “Density functional theory with dispersion corrections for supramolecular structures, aggregates, and complexes of (bio)organic molecules,” *Org. Biomol. Chem.*, vol. 5, no. 5, pp. 741–758, 2007.
- [67] W. Zhang, C. P. Chuu, J. K. Huang, C. H. Chen, M. L. Tsai, Y. H. Chang, C. T. Liang, Y. Z. Chen, Y. L. Chueh, J. H. He, M. Y. Chou, and L. J. Li, “Ultrahigh-gain photodetectors based on atomically thin graphene-mos2 heterostructures,” *Scientific Reports*, vol. 4, pp. 1–8, 2015.
- [68] E. V. Castro, K. S. Novoselov, S. V. Morozov, N. M. Peres, J. M. D. Santos, J. Nilsson, F. Guinea, A. K. Geim, and A. H. Neto, “Biased bilayer graphene: Semiconductor with a gap tunable by the electric field effect,” *Physical Review Letters*, vol. 99, pp. 8–11, 2007.
- [69] M. I. Katsnelson and A. Fasolino, “Graphene as a prototype crystalline membrane,” *Accounts of Chemical Research*, vol. 46, no. 1, pp. 97–105, 2013, PMID: 23072428.
- [70] S. Cahangirov, M. Topsakal, E. Aktürk, H. Şahin, and S. Ciraci, “Two- and one-dimensional honeycomb structures of silicon and germanium,” *Phys. Rev. Lett.*, vol. 102, p. 236804, Jun 2009.
- [71] W. Choi, N. Choudhary, G. H. Han, J. Park, D. Akinwande, and Y. H. Lee, “Recent development of two-dimensional transition metal dichalcogenides and their applications,” *Materials Today*, vol. 20, no. 3, pp. 116–130, Apr. 2017.

-
- [72] H.-Y. Chang, M. N. Yogeesh, R. Ghosh, A. Rai, A. Sanne, S. Yang, N. Lu, S. K. Banerjee, and D. Akinwande, “Large-area monolayer MoS for flexible low-power RF nanoelectronics in the GHz regime,” *Advanced Materials*, vol. 28, no. 9, pp. 1818–1823, Dec. 2015.
- [73] A. Castellanos-Gomez, M. Poot, G. A. Steele, H. S. J. van der Zant, N. Agraït, and G. Rubio-Bollinger, “Elastic properties of freely suspended MoSnanosheets,” *Advanced Materials*, vol. 24, no. 6, pp. 772–775, Jan. 2012.
- [74] T. Ohta, A. Bostwick, T. Seyller, K. Horn, and E. Rotenberg, “Controlling the electronic structure of bilayer graphene,” *Science*, vol. 313, no. 5789, pp. 951–954, Aug. 2006.
- [75] C. O. Girit, J. C. Meyer, R. Erni, M. D. Rossell, C. Kisielowski, L. Yang, C.-H. Park, M. F. Crommie, M. L. Cohen, S. G. Louie, and A. Zettl, “Graphene at the edge: Stability and dynamics,” *Science*, vol. 323, no. 5922, pp. 1705–1708, Mar. 2009.
- [76] G. Yang, L. Li, W. B. Lee, and M. C. Ng, “Structure of graphene and its disorders: a review,” *Science and Technology of Advanced Materials*, vol. 19, no. 1, pp. 613–648, Aug. 2018.
- [77] S. Trivedi, A. Srivastava, and R. Kurchania, “Silicene and germanene: A first principle study of electronic structure and effect of hydrogenation-passivation,” *Journal of Computational and Theoretical Nanoscience*, vol. 11, no. 3, pp. 781–788, Mar. 2014.
- [78] E. S. Kadantsev and P. Hawrylak, “Electronic structure of a single MoS2 monolayer,” *Solid State Communications*, vol. 152, no. 10, pp. 909–913, May 2012.
- [79] S. Larentis, B. Fallahazad, and E. Tutuc, “Field-effect transistors and intrinsic mobility in ultra-thin MoS2 layers,” *Applied Physics Letters*, vol. 101, no. 22, p. 223104, Nov. 2012.
- [80] Y. Guo, Y. Ji, H. Dong, L. Wang, and Y. Li, “Electronic and optical properties of defective MoS2 repaired by halogen atoms from first-principles study,” *AIP Advances*, vol. 9, no. 2, p. 025202, Feb. 2019.

-
- [81] B. Mortazavi, G. R. Berdiyev, M. Makaremi, and T. Rabczuk, “Mechanical responses of two-dimensional MoTe₂ pristine 2h, 1t and 1t2h heterostructure,” *Extreme Mechanics Letters*, vol. 20, pp. 65–72, Apr. 2018.
- [82] C. Ataca, H. Şahin, and S. Ciraci, “Stable, single-layer MX transition-metal oxides and dichalcogenides in a honeycomb-like structure,” *The Journal of Physical Chemistry C*, vol. 116, no. 16, pp. 8983–8999, Apr. 2012.
- [83] M. D. Bhatt, H. Kim, and G. Kim, “Various defects in graphene: a review,” *RSC Advances*, vol. 12, no. 33, pp. 21 520–21 547, 2022. [Online]. Available: <https://doi.org/10.1039/d2ra01436j>
- [84] J. Padilha, R. Amorim, A. Rocha, A. da Silva, and A. Fazzio, “Energetics and stability of vacancies in carbon nanotubes,” *Solid State Communications*, vol. 151, no. 6, pp. 482–486, Mar. 2011.
- [85] M. Saito, K. Yamashita, and T. Oda, “Magic numbers of graphene multivacancies,” *Japanese Journal of Applied Physics*, vol. 46, no. No. 47, pp. L1185–L1187, Nov. 2007.
- [86] R. Li, Y. Han, T. Hu, J. Dong, and Y. Kawazoe, “Self-healing monovacancy in low-buckled silicene studied by first-principles calculations,” *Physical Review B*, vol. 90, no. 4, Jul. 2014.
- [87] W. Amalia, P. Nurwantoro, and Sholihun, “Density-functional-theory calculations of structural and electronic properties of vacancies in monolayer hexagonal boron nitride (h-BN),” *Computational Condensed Matter*, vol. 18, p. e00354, Mar. 2019.
- [88] J. Zhou, W. Zhou, C. Guan, J. Shen, C. Ouyang, M. Lei, S. Shi, and W. Tang, “First-principles study of lithium intercalated bilayer graphene,” *Science China Physics, Mechanics and Astronomy*, vol. 55, no. 8, pp. 1376–1382, Jun. 2012.
- [89] J.-M. Tarascon and M. Armand, “Issues and challenges facing rechargeable lithium batteries,” *Nature*, vol. 414, no. 6861, pp. 359–367, Nov. 2001.
- [90] X. Zhao, J. E, G. Wu, Y. Deng, D. Han, B. Zhang, and Z. Zhang, “A review of studies using graphenes in energy conversion, energy storage and heat transfer development,” *Energy Conversion and Management*, vol. 184, pp. 581–599, 2019.

-
- [91] M. Kühne, F. Börrnert, S. Fecher, M. Ghorbani-Asl, J. Biskupek, D. Samuelis, A. V. Krasheninnikov, U. Kaiser, and J. H. Smet, “Reversible superdense ordering of lithium between two graphene sheets,” *Nature*, vol. 564, no. 7735, pp. 234–239, Nov. 2018.
- [92] K. Tanwar, X. Tan, S. C. Smith, and Y. I. Chen, “Huge lithium storage in 2d bilayer structures with point defects,” *The Journal of Physical Chemistry C*, vol. 125, no. 43, pp. 23 597–23 603, Oct. 2021.
- [93] J. P. Perdew, K. Burke, and M. Ernzerhof, “Generalized gradient approximation made simple,” *Physical Review Letters*, vol. 77, pp. 3865–3868, 1996.
- [94] Z. Cheng, X. Zhang, H. Zhang, H. Liu, X. Yu, X. Dai, G. Liu, and G. Chen, “Large vacancy-defective graphene for enhanced lithium storage,” *Carbon Trends*, vol. 10, p. 100237, Mar. 2023. [Online]. Available: <https://doi.org/10.1016/j.cartre.2022.100237>
- [95] A. C. Ferrari, J. C. Meyer, V. Scardaci, C. Casiraghi, M. Lazzeri, F. Mauri, S. Piscanec, D. Jiang, K. S. Novoselov, S. Roth, and A. K. Geim, “Raman spectrum of graphene and graphene layers,” *Phys. Rev. Lett.*, vol. 97, p. 187401, Oct 2006.
- [96] Z. Liu, K. Suenaga, P. J. F. Harris, and S. Iijima, “Open and closed edges of graphene layers,” *Phys. Rev. Lett.*, vol. 102, p. 015501, Jan 2009.
- [97] T. Li, X. Tang, Z. Liu, and P. Zhang, “Effect of intrinsic defects on electronic structure of bilayer graphene: First-principles calculations,” *Physica E: Low-dimensional Systems and Nanostructures*, vol. 43, no. 9, pp. 1597–1601, Jul. 2011.
- [98] S. Sangavi, N. Santhanamoorthi, and S. Vijayakumar, “Density functional theory study on the adsorption of alkali metal ions with pristine and defected graphene sheet,” *Molecular Physics*, vol. 117, no. 4, pp. 462–473, Sep. 2018. [Online]. Available: <https://doi.org/10.1080/00268976.2018.1523480>
- [99] X. Fan, W. Zheng, and J.-L. Kuo, “Adsorption and diffusion of li on pristine and defective graphene,” *ACS Applied Materials Interfaces*, vol. 4, no. 5, pp. 2432–2438, May 2012.

-
- [100] W. Shi, Z. Wang, Z. Li, and Y. Fu, “Electric field enhanced adsorption and diffusion of adatoms in MoS₂ monolayer,” *Materials Chemistry and Physics*, vol. 183, pp. 392–397, Nov. 2016.
- [101] M. Andersen, L. Hornekær, and B. Hammer, “Understanding intercalation structures formed under graphene on ir(111),” *Phys. Rev. B*, vol. 90, p. 155428, Oct 2014.
- [102] Y. Okamoto, “Density functional theory calculations of lithium adsorption and insertion to defect-free and defective graphene,” *The Journal of Physical Chemistry C*, vol. 120, no. 26, pp. 14 009–14 014, Jun. 2016.
- [103] A. J. Jacobson and L. F. Nazar, *Intercalation Chemistry-Encyclopedia of Inorganic Chemistry*. John Wiley & Sons, Ltd, Dec. 2011.
- [104] Q. Peng, K. Hu, B. Sa, J. Zhou, B. Wu, X. Hou, and Z. Sun, “Unexpected elastic isotropy in a black phosphorene/TiC₂ van der waals heterostructure with flexible li-ion battery anode applications,” *Nano Research*, vol. 10, no. 9, pp. 3136–3150, May 2017. [Online]. Available: <https://doi.org/10.1007/s12274-017-1531-5>
- [105] S. Fu, D. Wang, Z. Ma, G. Liu, X. Zhu, M. Yan, and Y. Fu, “The first-principles study on the halogen-doped graphene/mos₂ heterojunction,” *Solid State Communications*, vol. 334-335, p. 114366, 2021.
- [106] S. Tang, W. Wu, X. Xie, X. Li, and J. Gu, “Band gap opening of bilayer graphene by graphene oxide support doping,” *RSC Advances*, vol. 7, pp. 9862–9871, 2017.
- [107] M. Tayyab, A. Hussain, W. Adil, S. Nabi, and Q. ul Ain Asif, “Band-gap engineering of graphene by al doping and adsorption of be and br on impurity: A computational study,” *Computational Condensed Matter*, vol. 23, p. e00463, 2020.
- [108] B. R. Matis, J. S. Burgess, F. A. Bulat, A. L. Friedman, B. H. Houston, and J. W. Baldwin, “Surface doping and band gap tunability in hydrogenated graphene,” *ACS Nano*, vol. 6, pp. 17–22, 2012.
- [109] T. Hirahara, R. Ebisuoka, T. Oka, T. Nakasuga, S. Tajima, K. Watanabe, T. Taniguchi, and R. Yagi, “Multilayer graphene shows intrinsic resistance peaks in the carrier density dependence,” *Scientific Reports*, vol. 8, pp. 1–3, 2018.

-
- [110] Y. Zhang, T. T. Tang, C. Girit, Z. Hao, M. C. Martin, A. Zettl, M. F. Crommie, Y. R. Shen, and F. Wang, "Direct observation of a widely tunable bandgap in bilayer graphene," *Nature*, vol. 459, pp. 820–823, 2009.
- [111] X. Cao, J. J. Shi, M. Zhang, X. H. Jiang, H. X. Zhong, P. Huang, Y. M. Ding, and M. Wu, "Band gap opening of graphene by forming heterojunctions with the 2d carbonitrides nitrogenated holey graphene, g-c3n4, and g-cn: Electric field effect," *Journal of Physical Chemistry C*, vol. 120, pp. 11 299–11 305, 2016.
- [112] M. Gmitra and J. Fabian, "Proximity effects in bilayer graphene on monolayer wse2: Field-effect spin valley locking, spin-orbit valve, and spin transistor," *Physical Review Letters*, vol. 119, pp. 2–6, 2017.
- [113] S. Singh, C. Espejo, and A. H. Romero, "Structural, electronic, vibrational, and elastic properties of graphene/mos2 bilayer heterostructures," *Physical Review B*, vol. 98, pp. 1–10, 2018.
- [114] X. Yu, G. Zhao, S. Gong, C. Liu, C. Wu, P. Lyu, G. Maurin, and N. Zhang, "Design of mos2/graphene van der waals heterostructure as highly efficient and stable electrocatalyst for hydrogen evolution in acidic and alkaline media," *ACS Applied Materials and Interfaces*, vol. 12, pp. 24 777–24 785, 2020.
- [115] Z. Yin, H. Li, H. Li, L. Jiang, Y. Shi, Y. Sun, G. Lu, Q. Zhang, X. Chen, and H. Zhang, "Single-layer mos 2 phototransistors," *ACS Nano*, vol. 6, pp. 74–80, 2012.
- [116] S. A. Han, R. Bhatia, and S. W. Kim, "Synthesis, properties and potential applications of two-dimensional transition metal dichalcogenides," *Nano Convergence*, vol. 2, 2015.
- [117] A. Splendiani, L. Sun, Y. Zhang, T. Li, J. Kim, C. Y. Chim, G. Galli, and F. Wang, "Emerging photoluminescence in monolayer mos2," *Nano Letters*, vol. 10, pp. 1271–1275, 2010.
- [118] J. Nevalaita and P. Koskinen, "Atlas for the properties of elemental two-dimensional metals," *Physical Review B*, vol. 97, pp. 1–11, 2018.
- [119] K. Zhang, X. Fang, Y. Wang, Y. Wan, Q. Song, W. Zhai, Y. Li, G. Ran, Y. Ye, and L. Dai, "Ultrasensitive near-infrared photodetectors based on a graphene-

-
- mote2-graphene vertical van der waals heterostructure,” *ACS Applied Materials and Interfaces*, vol. 9, pp. 5392–5398, 2017.
- [120] K. Roy, M. Padmanabhan, S. Goswami, T. P. Sai, G. Ramalingam, S. Raghavan, and A. Ghosh, “Graphene-mos 2 hybrid structures for multifunctional photoreponsive memory devices,” *Nature Nanotechnology*, vol. 8, pp. 826–830, 2013.
- [121] S. W. Han, H. Kwon, S. K. Kim, S. Ryu, W. S. Yun, D. H. Kim, J. H. Hwang, J. S. Kang, J. Baik, H. J. Shin, and S. C. Hong, “Band-gap transition induced by interlayer van der waals interaction in mos2,” *Physical Review B - Condensed Matter and Materials Physics*, vol. 84, pp. 17–22, 2011.
- [122] M. Gmitra, D. Kochan, P. Högl, and J. Fabian, “Trivial and inverted dirac bands and the emergence of quantum spin hall states in graphene on transition-metal dichalcogenides,” *Physical Review B*, vol. 93, pp. 1–10, 2016.
- [123] C. S. Lee and T. H. Kim, “Large-scale preparation of mos2/graphene composites for electrochemical detection of morin,” *ACS Applied Nano Materials*, vol. 4, pp. 6668–6677, 2021.
- [124] X. Wen, H. Chen, T. Wu, Z. Yu, Q. Yang, J. Deng, Z. Liu, X. Guo, J. Guan, X. Zhang, Y. Gong, J. Yuan, Z. Zhang, C. Yi, X. Guo, P. M. Ajayan, W. Zhuang, Z. Liu, J. Lou, and J. Zheng, “Ultrafast probes of electron-hole transitions between two atomic layers,” *Nature Communications*, vol. 9, pp. 1–9, 2018.
- [125] Y. Liu, C. Liu, X. Wang, L. He, X. Wan, Y. Xu, Y. Shi, R. Zhang, and F. Wang, “Photoresponsivity of an all-semimetal heterostructure based on graphene and wte2,” *Scientific Reports*, vol. 8, pp. 1–7, 2018.
- [126] A. Gao, E. Liu, M. Long, W. Zhou, Y. Wang, T. Xia, W. Hu, B. Wang, and F. Miao, “Gate-tunable rectification inversion and photovoltaic detection in graphene/wse2 heterostructures,” *Applied Physics Letters*, vol. 108, p. 223501, 5 2016, doi: 10.1063/1.4953152.
- [127] D. Akinwande, N. Petrone, and J. Hone, “Two-dimensional flexible nanoelectronics,” *Nature Communications*, vol. 5, 2014.
- [128] N. Huo, Z. Wei, X. Meng, J. Kang, F. Wu, S. S. Li, S. H. Wei, and J. Li, “Interlayer coupling and optoelectronic properties of ultrathin two-dimensional

-
- heterostructures based on graphene, mos2 and ws2,” *Journal of Materials Chemistry C*, vol. 3, pp. 5467–5473, 2015.
- [129] M. Weinert, E. Wimmer, and A. J. Freeman, “Total-energy all-electron density functional method for bulk solids and surfaces,” *PHYSICAL REVIEW B*, vol. 26, p. 4571 – 4578, 1982.
- [130] T. Bučko, J. Hafner, S. Lebègue, and J. G. Ángyán, “Improved description of the structure of molecular and layered crystals: Ab initio dft calculations with van der waals corrections,” *Journal of Physical Chemistry A*, vol. 114, pp. 11 814–11 824, 11 2010.
- [131] P. Tao, H.-H. Guo, T. Yang, and Z.-D. Zhang, “Stacking stability of MoS,” *Chinese Physics B*, vol. 23, no. 10, p. 106801, Oct. 2014.
- [132] F. A. Rasmussen and K. S. Thygesen, “Computational 2d materials database: Electronic structure of transition-metal dichalcogenides and oxides,” *The Journal of Physical Chemistry C*, vol. 119, no. 23, pp. 13 169–13 183, Jun. 2015.
- [133] B. Sachs, L. Britnell, T. O. Wehling, A. Eckmann, R. Jalil, B. D. Belle, A. I. Lichtenstein, M. I. Katsnelson, and K. S. Novoselov, “Doping mechanisms in graphene-MoShybrids,” *Applied Physics Letters*, vol. 103, no. 25, p. 251607, Dec. 2013.
- [134] A. K. Singh, P. Kumar, D. Late, A. Kumar, S. Patel, and J. Singh, “2d layered transition metal dichalcogenides (MoS₂): Synthesis, applications and theoretical aspects,” *Applied Materials Today*, vol. 13, pp. 242–270, Dec. 2018.
- [135] A. Ebnonnasir, B. Narayanan, S. Kodambaka, and C. V. Ciobanu, “Tunable MoSgraphene heterostructures,” *Applied Physics Letters*, vol. 105, no. 3, p. 031603, Jul. 2014.
- [136] B. Liu, L.-J. Wu, Y.-Q. Zhao, L.-Z. Wang, and M.-Q. Cai, “First-principles investigation of the schottky contact for the two-dimensional MoS and graphene heterostructure,” *RSC Advances*, vol. 6, no. 65, pp. 60 271–60 276, 2016.
- [137] X. Li, L. Tao, Z. Chen, H. Fang, X. Li, X. Wang, J.-B. Xu, and H. Zhu, “Graphene and related two-dimensional materials: Structure-property relationships for elec-

-
- tronics and optoelectronics,” *Applied Physics Reviews*, vol. 4, no. 2, p. 021306, 2017.
- [138] N. Tombros, C. Jozsa, M. Popinciuc, H. T. Jonkman, and B. J. V. Wees, “Electronic spin transport and spin precession in single graphene layers at room temperature,” *Nature*, vol. 448, pp. 571–574, 2007.
- [139] W. Han, K. Pi, K. M. McCreary, Y. Li, J. J. Wong, A. G. Swartz, and R. K. Kawakami, “Tunneling spin injection into single layer graphene,” *Physical Review Letters*, vol. 105, 10 2010.
- [140] M. Gmitra, D. Kochan, and J. Fabian, “Spin-orbit coupling in hydrogenated graphene,” *Physical Review Letters*, vol. 110, 6 2013.
- [141] C. K. Safeer, J. Ingla-Aynés, F. Herling, J. H. Garcia, M. Vila, N. Ontoso, M. R. Calvo, S. Roche, L. E. Hueso, and F. Casanova, “Room-temperature spin hall effect in graphene/mos2 van der waals heterostructures,” *Nano Letters*, vol. 19, pp. 1074–1082, 2019.
- [142] J. H. Garcia, M. Vila, A. W. Cummings, and S. Roche, “Spin transport in graphene/transition metal dichalcogenide heterostructures,” *Chemical Society Reviews*, vol. 47, pp. 3359–3379, 5 2018.
- [143] X. Liu, I. Balla, H. Bergeron, G. P. Campbell, M. J. Bedzyk, and M. C. Hersam, “Rotationally commensurate growth of mos2 on epitaxial graphene,” *ACS Nano*, vol. 10, pp. 1067–1075, 1 2016.
- [144] K. Zhang, X. Fang, Y. Wang, Y. Wan, Q. Song, W. Zhai, Y. Li, G. Ran, Y. Ye, and L. Dai, “Ultrasensitive near-infrared photodetectors based on a graphene-mote2-graphene vertical van der waals heterostructure,” *ACS Applied Materials and Interfaces*, vol. 9, pp. 5392–5398, 2017.
- [145] S. Agnoli, A. Ambrosetti, T. O. Menteş, A. Sala, A. Locatelli, P. L. Silvestrelli, M. Cattelan, S. Eichfeld, D. D. Deng, J. A. Robinson, J. Avila, C. Chen, and M. C. Asensio, “Unraveling the structural and electronic properties at the wse2-graphene interface for a rational design of van der waals heterostructures,” *ACS Applied Nano Materials*, vol. 1, pp. 1131–1140, 3 2018.

-
- [146] N. Li, T. Tang, J. Li, L. Luo, C. Li, J. Shen, and J. Yao, “Highly sensitive biosensor with graphene-mos2 heterostructure based on photonic spin hall effect,” *Journal of Magnetism and Magnetic Materials*, vol. 484, pp. 445–450, 8 2019.
- [147] G. Chen and J. L. Lado, “Tunable moire spinons in magnetically encapsulated twisted van der waals quantum spin liquids,” *Physical Review Research*, vol. 3, 2021.
- [148] J. H. Garcia, A. W. Cummings, and S. Roche, “Spin hall effect and weak antilocalization in graphene/transition metal dichalcogenide heterostructures,” *Nano Letters*, vol. 17, pp. 5078–5083, 8 2017.
- [149] Y. Ma, Y. Dai, M. Guo, C. Niu, and B. Huang, “Graphene adhesion on MoS2 monolayer: An ab initio study,” *Nanoscale*, vol. 3, no. 9, p. 3883, 2011.
- [150] A. M. Pradipto, T. Akiyama, T. Ito, and K. Nakamura, “External electric field driven modification of the anomalous and spin hall conductivities in fe thin films on mgo(001),” *Phys. Rev. B*, vol. 97, p. 024401, Jan 2018.
- [151] X. Liu and Z. Li, “Electric field and strain effect on graphene-mos2 hybrid structure: Ab initio calculations,” *Journal of Physical Chemistry Letters*, vol. 6, pp. 3269–3275, 8 2015.
- [152] H. J. Conley, B. Wang, J. I. Ziegler, R. F. Haglund, S. T. Pantelides, and K. I. Bolotin, “Bandgap engineering of strained monolayer and bilayer mos2,” *Nano Letters*, vol. 13, pp. 3626–3630, 8 2013.
- [153] A. Dyrdał and J. Barnaś, “Spin hall effect in aa-stacked bilayer graphene,” *Solid State Communications*, vol. 188, pp. 27–31, 2014.
- [154] P. Tiwari, M. K. Jat, A. Udupa, D. S. Narang, K. Watanabe, T. Taniguchi, D. Sen, and A. Bid, “Observation spin-splitting,” *npj 2D Materials and Applications*, vol. 6, 12 2022.
- [155] G. Y. Guo, S. Murakami, T.-W. Chen, and N. Nagaosa, “Intrinsic spin hall effect in platinum: First-principles calculations,” *Phys. Rev. Lett.*, vol. 100, p. 096401, Mar 2008.

List of Publications

1. Hastuti, D. P., Nawa, K., and Nakamura, K. (2023) Electronic Structures of graphene-MoS₂ Heterostructure: Effects of Stacking Orientation, Element Substitution, and Interlayer Distance. *Indonesian Journal of Chemistry*, 23 (1), 140 - 147. doi:10.22146/ijc.75538
2. Hastuti, D. P., Amalia, W., Priska, Z., Nurwantoro, P., and Sholihun. (2020). First-principles density-functional-theory calculations of formation and dissociation energies in germanene multivacancies. *Materials Today Communications*, 100754. doi:10.1016/j.mtcomm.2019.1007
3. Hastuti, D. P., Nurwantoro, P., and Sholihun. (2019). Stability study of germanene vacancies: The first-principles calculations. *Materials Today Communications*, 19, 459–463. doi:10.1016/j.mtcomm.2019.04.0

List of Presentations

1. Dian Putri Hastuti, Kenji Nawa, Kohji Nakamura, "Effect of External Electric Field in Tuning Spin Hall Conductivity of Graphene/MoS₂ van der Waals Heterostructure: A First-Principles Study", 11th International Symposium on Metallic Multilayers (MML 2023), Seoul, Korea 24-28th 2023.
2. Dian Putri Hastuti, Kenji Nawa, Kohji Nakamura, "The Effect of External Electric Field on Electronic and Spin Properties of MoS₂-graphene van der Waals Heterostructures", *The JSAP Spring meeting*, Tokyo, March 15-18th 2023.
3. Dian Putri Hastuti, Kenji Nawa, Kohji Nakamura, "Electronic structures of graphene-MoS₂ heterostructure from first principles: The effects of stacking orientation, element substitution, and interlayer distance", *The IEEE Magnetic Society Nagoya Section*, Nagoya, February 2nd 2023.
4. Dian Putri Hastuti, Kenji Nawa, Kohji Nakamura, "Tunable Optical Properties in MoS₂/WS₂ Heterostructure by External Electric Field", *The JSAP Autumn meeting*, Sendai, September 20-23rd 2022.
5. Dian Putri Hastuti, Kenji Nawa, Kohji Nakamura, "Controllable Electronic and Spin Properties of MoS₂-based van der Waals heterostructures", *The 24th International Colloquium on Magnetic Films and Surfaces (ICMFS-2022)*, Okinawa, July 10-15th 2022.
6. Dian Putri Hastuti, Kenji Nawa, Kohji Nakamura, "First-principles Study of Structural and Electronic Properties of graphene-MoS₂ Heterostructure", *The JSAP Autumn meeting*, Virtual meeting, September 13th 2021.